

pop-cosmos: Forward modeling KiDS-1000 redshift distributions using realistic galaxy populations

BORIS LEISTEDT,¹ HIRANYA V. PEIRIS,^{2,3,4} ANIK HALDER,^{2,5} STEPHEN THORP,^{2,4} DANIEL J. MORTLOCK,^{1,6}
ARTHUR LOUREIRO,^{4,1} JUSTIN ALSING,⁴ GURJEET JAGWANI,^{2,7} MADALINA N. TUDORACHE,² SINAN DEGER,²
JOEL LEJA,^{8,9,10} BENEDICT VAN DEN BUSSCHE,² ANGUS H. WRIGHT,¹¹ SHUN-SHENG LI,^{12,13} KONRAD KUIJKEN,¹³ AND
HENDRIK HILDEBRANDT¹¹

¹*Astrophysics Group, Imperial College London, Blackett Laboratory, Prince Consort Road, London, SW7 2AZ, UK*

²*Institute of Astronomy and Kavli Institute for Cosmology, University of Cambridge, Madingley Road, Cambridge CB3 0HA, UK*

³*Cavendish Laboratory, Department of Physics, University of Cambridge, JJ Thomson Avenue, Cambridge, CB3 0HE, UK*

⁴*The Oskar Klein Centre, Department of Physics, Stockholm University, AlbaNova University Centre, SE 106 91 Stockholm, Sweden*

⁵*Jesus College, Jesus Lane, Cambridge, CB5 8BL, UK*

⁶*Department of Mathematics, Imperial College London, London SW7 2AZ, UK*

⁷*Research Computing Services, University of Cambridge, Roger Needham Building, 7 JJ Thomson Ave, Cambridge CB3 0RB, UK*

⁸*Department of Astronomy & Astrophysics, The Pennsylvania State University, University Park, PA 16802, USA*

⁹*Institute for Computational & Data Sciences, The Pennsylvania State University, University Park, PA 16802, USA*

¹⁰*Institute for Gravitation & the Cosmos, The Pennsylvania State University, University Park, PA 16802, USA*

¹¹*Ruhr University Bochum, Faculty of Physics and Astronomy, Astronomical Institute (AIRUB), German Centre for Cosmological Lensing (GCCL), 44780 Bochum, Germany*

¹²*Kavli Institute for Particle Astrophysics and Cosmology (KIPAC), SLAC National Accelerator Laboratory and Stanford University, Stanford, CA 94305, USA*

¹³*Leiden Observatory, Leiden University, PO Box 9513, 2300 RA Leiden, The Netherlands*

Submitted to ApJ

ABSTRACT

The accuracy of the cosmological constraints from Stage IV galaxy surveys will be limited by how well the galaxy redshift distributions can be inferred. We have addressed this challenging problem for the Kilo-Degree Survey (KiDS) cosmic shear sample by developing a forward-modeling framework with two main ingredients: (1) the **pop-cosmos** generative model for the evolving galaxy population, calibrated on *Spitzer* IRAC *Ch. 1* < 26 galaxies from COSMOS2020; and (2) a data model for noise and selection, machine-learned from the SURFS-based KiDS-Legacy-Like Simulations (SKILLS). Applying KiDS tomographic binning to our synthetic photometric data, we infer redshift distributions in each of five bins directly from the population and data models, bypassing the need for spectroscopic reweighting. Keeping the data model fixed, we compare results using two different galaxy population models: **pop-cosmos**; and **shark**, the semi-analytic galaxy formation model used in SKILLS. In the first ($0.1 < z < 0.3$) and last ($0.9 < z < 1.2$) tomographic bins we find systematic differences in the mean redshifts of $\Delta z \sim 0.05$ - 0.1 , comparable to the reported uncertainties from spectroscopic reweighting methods. This work paves the way for accurate redshift distribution calibration for Stage IV surveys directly through forward modeling, thus providing an independent cross-check on spectroscopic-based calibrations which avoids their selection biases and incompleteness. We will use the **pop-cosmos** redshift distributions in an upcoming full KiDS cosmology reanalysis.

Keywords: Galaxy evolution (594); Galaxy photometry (611); Redshift surveys (1378)

1. INTRODUCTION

The extraction of cosmological information from galaxy surveys relies critically on our ability to model

and understand the galaxy populations we observe. Modern wide-field surveys like the Kilo-Degree Survey (KiDS; J. T. A. de Jong et al. 2013), Dark Energy Survey (DES; Dark Energy Survey Collaboration 2005), and Hyper Suprime-Cam Subaru Strategic Program (HSC SSP; H. Aihara et al. 2018) provide unprecedented statistical power for weak gravitational lensing measurements. However, this power can only be fully real-

ized by accurately characterizing the observed galaxy samples, in particular their redshift distributions, $n(z)$ (see e.g. R. Mandelbaum 2018; J. A. Newman & D. Gruen 2022). Traditional approaches to this problem have relied on empirical calibrations using spectroscopic samples. While spectroscopic calibrations provide direct measurements, they suffer from incompleteness and their own selection biases. In this work, we reframe this as *forward-modeling redshift calibration*: rather than directly re-weighting spectroscopic samples to estimate $n(z)$, we start from a generative model of the galaxy population that reproduces observed color–redshift relations, forward-model it through a realistic KiDS data model, and then apply exactly the same tomographic binning procedure as for the data.

Image simulations are the ideal tool to forward model photometric data since they offer complete control over the input population and can accurately capture all known observational effects. The SURFS-based KiDS-Legacy-Like Simulations (SKiLLS; S.-S. Li et al. 2023a) exemplify this approach: by injecting galaxies from the *shark* semi-analytic model (C. d. P. Lagos et al. 2018) into synthetic images with the GALSIM image simulation software (B. T. P. Rowe et al. 2015), incorporating realistic point spread functions, backgrounds, and noise, SKiLLS enabled validation of the KiDS-1000 self-organizing map redshift calibration (H. Hildebrandt et al. 2021; A. H. Wright et al. 2025a) and the KiDS shear measurement pipelines¹⁴ (S.-S. Li et al. 2023b; M. Yoon et al. 2025). However, generating $\sim 100 \text{ deg}^2$ of mock images required a prohibitive amount of computing time. Image simulations have also been employed within forward modeling frameworks to constrain redshift distributions and luminosity functions (e.g. J. Herbel et al. 2017; L. Tortorelli et al. 2018; L. Tortorelli et al. 2020; B. Moser et al. 2024; S. Fischbacher et al. 2025a,b) using the Ultra Fast Image Generator (UFIG; J. Bergé et al. 2013; S. Fischbacher et al. 2025c).

Recent advances in machine learning¹⁵ and generative modeling make it possible to construct data-driven population models that can be used to rapidly generate realistic galaxy catalogs while maintaining the flexibility for exploration of systematic uncertainties (see J. Alsing et al. 2023). This type of approach has been used to produce mock galaxy imaging (e.g. J. Bergé et al. 2013; J. Herbel et al. 2017; B. Moser et al. 2024; S. Fischbacher et al. 2025b,a; L. Tortorelli et al. 2025), pro-

vide GPU-based SPS libraries (e.g. A. P. Hearin et al. 2023; A. Alarcon et al. 2023, 2025), and generate forward models for spectroscopic data (e.g. C. Hahn et al. 2023, 2024). Our contribution to this field has been to develop the *pop-cosmos* framework (J. Alsing et al. 2024; S. Thorp et al. 2024, 2025; S. Deger et al. 2025), which is the primary tool used in this paper. By training score-based diffusion models on deep photometric data from the Cosmic Evolution Survey (COSMOS; N. Scoville et al. 2007), *pop-cosmos* encodes galaxies with realistic correlations between their physical properties and observed photometry. The model operates in the space of stellar population synthesis (SPS; see e.g. C. Conroy 2013; K. G. Iyer et al. 2026) parameters, enabling direct inference of physical properties while maintaining consistency with observed color and magnitude distributions. Crucially, *pop-cosmos* achieves excellent photometric redshift performance (estimating galaxy distances from multi-band colors rather than spectra; S. Thorp et al. 2024, 2025).

In this work, we develop a forward modeling framework for inferring the tomographic redshift distributions of galaxies in the KiDS-1000 weak lensing catalog (K. Kuijken et al. 2019; B. Giblin et al. 2021), based on the KiDS data and SKiLLS image simulations introduced in Section 2. This framework combines the *pop-cosmos* population model with a machine-learned data model, trained on SKiLLS, that captures the transformation from noiseless galaxy photometry to realistic survey observations, including photometric noise, detection thresholds, and measurement uncertainties (described in detail in Section 3). This allows us to rapidly generate mock KiDS observations for any input galaxy populations, including *pop-cosmos* and *shark*. We then apply our framework to estimate redshift distributions for the KiDS-1000 tomographic bins, demonstrating how they are affected by the choice of underlying galaxy population. We discuss these results in Section 5 and summarise our conclusions in Section 6. This work presents the first application of *pop-cosmos* to a galaxy survey beyond the COSMOS dataset on which it was originally calibrated, complementing A. Halder et al. (2026, hereafter H26), who apply *pop-cosmos* to individual KiDS-1000 galaxies for the inference of individual galaxy properties.

All magnitudes in this work are given in the AB system. The *pop-cosmos* model assumes a flat Λ CDM cosmology with $H_0 = 67.66 \text{ km s}^{-1} \text{ Mpc}^{-1}$ and $\Omega_m = 0.3097$ (Planck Collaboration et al. 2020), while SKiLLS assumes a flat Λ CDM cosmology with $H_0 = 67.51 \text{ km s}^{-1} \text{ Mpc}^{-1}$ and $\Omega_m = 0.3121$ (Planck Collaboration et al. 2016).

2. DATA

In this section we describe the KiDS DR4 data and the galaxy samples we consider (Section 2.1). We also describe the SKiLLS image simulations (Section 2.2).

¹⁴ Image simulations have been also been used by other major weak lensing surveys to calibrate shear measurements and deblending strategies (see e.g. R. Mandelbaum et al. 2018; X. Li et al. 2022; N. MacCrann et al. 2022).

¹⁵ Machine learning refers to computational methods that learn patterns from data without explicit programming. In our context, this includes generative models (synthesizing realistic galaxy properties) and supervised models (learning mappings between observables; e.g., noiseless to noisy photometry).

2.1. *KiDS data*

The KiDS Data Release 4 (DR4; K. Kuijken et al. 2019) covers 1022 deg² of optical imaging in four bands (*ugri*) obtained with the OmegaCAM wide-field imager (K. Kuijken et al. 2002; K. Kuijken 2011) on the VLT Survey Telescope (VST; M. Arnaboldi et al. 1998; M. Capaccioli & P. Schipani 2011). The survey footprint consists of two main regions: KiDS-North (~ 450 deg²) overlapping with the Galaxy and Mass Assembly (GAMA) survey (S. P. Driver et al. 2009); and KiDS-South (~ 550 deg²) overlapping with the 2 degree Field Galaxy Redshift Survey (2dFGRS; M. Colless et al. 2001). The median seeing ranges from 0.70'' in *r*-band to 1.00'' in *u*-band. The *r*-band limiting magnitude is ~ 25.0 (5σ in a 2'' aperture). KiDS DR4 provides photometry for $\sim 10^8$ sources using two complementary approaches: Gaussian Aperture and PSF (GAaP; K. Kuijken 2008) photometry for accurate colors; and Source Extractor (E. Bertin & S. Arnouts 1996) AUTO magnitudes for fluxes. Detection and star-galaxy separation are performed in the *r*-band, with sources required to have signal-to-noise ratio greater than 5 to be considered as detected. The nine-band (*ugriZYZHK_s*) photometric catalog is created by combining KiDS optical data with near-infrared data from the VISTA Kilo-degree Infrared Galaxy survey (VIKING; A. Edge et al. 2013), enabling improved photometric redshift estimation (H. Hildebrandt et al. 2021).

Weak-lensing studies use the KiDS-1000 source sample (B. Giblin et al. 2021), which consists of $\sim 2.1 \times 10^6$ galaxies from DR4 with robust shape measurements obtained with *lensfit* (L. Miller et al. 2013). These galaxies are divided into five tomographic bins using Bayesian Photo-Z (BPZ; N. Benítez 2000) photometric redshifts (A. H. Wright et al. 2019), with bin edges at redshifts of 0.1, 0.3, 0.5, 0.7, 0.9 and 1.2. Additional quality cuts remove spurious detections near bright stars, in masked regions, and at survey boundaries, resulting in an effective area of 777.4 deg² for cosmological analyses.

Unfortunately, some of the information required to construct the KiDS-1000 selection step-by-step from the DR4 catalog is not publicly available. Therefore, to support our analysis, we cross-matched the KiDS DR4 public catalogs with the KiDS-1000 science catalog to obtain the KiDS-1000 flag, a binary indicator of which galaxies pass the selection criteria for weak lensing analysis, along with their associated *lensfit* weight (B. Giblin et al. 2021)¹⁶.

¹⁶ Additionally, we cross-matched with internal (non-public) catalogs, kindly provided by the KiDS team, which contain photometric uncertainties for galaxies with negative measured fluxes. These were not preserved in the ESO public DR4, but were essential for reproducing both the selection function and the complete noise properties of the KiDS photometry. In particular, to handle missing data in the DR4 catalogs, which appear flagged by 99s (flux signal-to-noise ratio lower than one) or -99s (no

The KiDS DR4 catalog applies corrections for Galactic extinction using the D. J. Schlegel et al. (1998) $E(B-V)$ maps with E. F. Schlafly & D. P. Finkbeiner (2011) extinction coefficients, and photometric zero-point calibrations tied to Gaia DR2 using stellar locus regression (K. Kuijken et al. 2019). These corrections are already incorporated into the released GAaP magnitudes, which are provided as dereddened, calibrated apparent magnitudes. However, the catalog employs a two-magnitude system that requires aperture correction to recover total galaxy fluxes. The AUTO magnitude in the *r*-band is Kron-like (R. G. Kron 1980; E. Bertin & S. Arnouts 1996) and approximates the total light of galaxies, while the GAaP magnitudes across all nine bands (*ugriZYZHK_s*) are aperture-matched and PSF-corrected across bands. The latter provide accurate colors, but underestimate total fluxes for extended sources (since the aperture size is constrained to avoid contamination from neighboring objects; K. Kuijken 2008; K. Kuijken et al. 2019). To obtain total flux estimates in bands other than *r*, we apply the aperture correction by combining the *r*-band AUTO magnitude with GAaP colors (A. H. Wright et al. 2019). In band $b \in \{u, g, r, i, Z, Y, J, H, K_s\}$ this gives

$$\hat{F}_{b_{\text{GAaP}}}^{\text{corrected}} = \hat{F}_{b_{\text{GAaP}}} \frac{\hat{F}_{r_{\text{AUTO}}}}{\hat{F}_{r_{\text{GAaP}}}}. \quad (1)$$

The resultant fractional uncertainty is given by the quadrature sum

$$\left(\frac{\sigma_{b_{\text{GAaP}}}^{\text{corrected}}}{\hat{F}_{b_{\text{GAaP}}}^{\text{corrected}}} \right)^2 = \left(\frac{\sigma_{b_{\text{GAaP}}}}{\hat{F}_{b_{\text{GAaP}}}} \right)^2 + \left(\frac{\sigma_{r_{\text{AUTO}}}}{\hat{F}_{r_{\text{AUTO}}}} \right)^2 + \left(\frac{\sigma_{r_{\text{GAaP}}}}{\hat{F}_{r_{\text{GAaP}}}} \right)^2. \quad (2)$$

This correction procedure assumes no color gradients within galaxies, an assumption which has been tested by comparing GAaP fluxes measured with different aperture sizes (K. Kuijken et al. 2019). In our approach, we jointly model the *r*-band AUTO magnitude and the *ugriZYZHK_s* aperture-corrected GAaP magnitudes. This choice is supported by the robust photometric redshifts obtained by H26 by analysing the same photometry through SED fitting under the pop-cosmos prior¹⁷.

data), we implemented a resampling strategy that draws missing flux values from the flux uncertainty distributions. This ensures physically plausible imputation while maintaining the statistical properties of the data. This limitation of the ESO database was fixed for DR5.

¹⁷ For bright galaxies the combination of GAaP colors and Kron-like AUTO magnitudes can lead to a modest underestimation of the total flux for very extended sources (A. W. Graham & S. P. Driver 2005), such as luminous red galaxies (LRGs). This effect has been investigated in detail in the companion analysis of H26, who show that it can induce small but measurable biases in photometric redshifts for DESI LRGs when using KiDS photometry alone (see section 4.1 of H26). In the present work, however, we focus on the KiDS-1000 weak-lensing

2.2. Image simulations

The SKiLLS simulations (S.-S. Li et al. 2023a) provide realistic mock observations designed to match the properties of the KiDS data (building on the earlier KiDS simulations by I. Fenech Conti et al. 2017 and A. Kannawadi et al. 2019). These simulations combine cosmologically representative galaxy populations with observationally calibrated morphologies to create synthetic images that capture the complexity of the survey selection function. The galaxy population underlying SKiLLS comes from the SURFS-*shark* framework, which couples N -body simulations from the Synthetic Universe For Surveys (SURFS; P. J. Elahi et al. 2018) project with the *shark* semi-analytic galaxy formation model (C. d. P. Lagos et al. 2018). *shark* predicts galaxy properties including stellar masses, star formation histories, metallicities, and active galactic nucleus (AGN) activity, based on physical prescriptions for gas cooling, star formation, feedback, and mergers.

Multi-band photometry is generated using the ProSpect SPS code (A. S. G. Robotham et al. 2020), with the S. Charlot & S. M. Fall (2000) dust attenuation model and D. A. Dale et al. (2014) dust emission templates. A key feature of SKiLLS is the incorporation of realistic galaxy morphologies learned from Hubble Space Telescope (HST) observations in the COSMOS field (R. L. Griffith et al. 2012). This is based on vine copulas (see e.g. H. Joe 2014; C. Czado 2019) to capture the correlations between morphological parameters (size, ellipticity, Sérsic index) and other galaxy properties (magnitude, color, redshift), extending to magnitudes and redshifts beyond the HST sample. The image simulations inject these galaxies into realistic KiDS-like images, including PSFs, sky backgrounds, and noise properties matched to the survey data (S.-S. Li et al. 2023a). Galaxies are distributed with realistic clustering following the dark matter halos from the SURFS N -body simulations (P. J. Elahi et al. 2018). An empirical correction based on stellar mass-to-light ratios ensures the final galaxy number counts match observations in the COSMOS2015 dataset (I. Davidzon et al. 2017). The simulated images are processed through the same pipeline used for real KiDS data, resulting in realistic catalogs with identical data products, including GAaP and AUTO photometry, shape measurements, and photometric redshifts.

The SKiLLS noise model assumes Gaussian distributions for pixel noise. For optical bands, the noise properties are calibrated from Astro-WISE weight maps

source sample, which is dominated by fainter and less extended galaxies near the survey flux limit and strongly down-weighted by the *lensfit* scheme at high luminosities. Consequently, the specific GAaP-AUTO flux bias that affects bright LRGs is expected to have a negligible impact on the tomographic source redshift distributions.

(J. P. McFarland et al. 2013) with an empirical boost factor of ~ 1.145 to account for the re-gridding process (S.-S. Li et al. 2023a). For the VIKING infrared bands the noise modeling is simplified: rather than simulating the complex multi-exposure paw-print structure, SKiLLS uses single images per tile with noise levels derived by stacking flat-field images from overlapping paw-prints and taking median values. This simplified approach maintains realistic photometric properties while reducing computational overhead. The noise model has been validated by comparing the simulated GAaP limiting magnitudes to data, showing agreement within 0.1 mag for optical bands and somewhat larger scatter for NIR bands (S.-S. Li et al. 2023a).

For this work, we use both the output measurement catalogs containing 2×10^6 detected galaxies, and the input truth catalogs containing the noiseless properties of all injected galaxies. The availability of matched input-output pairs enables us to train our data model on the complex transformation between noiseless fluxes and noisy data, including detection probabilities, photometric scatter, and measurement biases. The simulations cover 100 deg^2 with depth variations representative of the full KiDS footprint, providing a comprehensive training set for our data model. To ensure a consistent treatment of noisy measurements, we apply to the simulated low signal-to-noise fluxes exactly the same resampling algorithm that we used for the real DR4 data, as described in the previous section.

3. MODELING

Our forward model for KiDS consists of five ingredients, which are applied in succession when constructing mock redshift distributions for the tomographic bins: a population model (Section 3.1); a data model (Section 3.2); selection and weighting (Sections 3.4 and 3.5); and a photometric redshift estimator (Section 3.3). Taken together, these ingredients define our forward-modeling redshift calibration: they allow us to start from a generative model of the galaxy population, create KiDS-like mock observations that pass the same tomographic binning as the data, and then read off the underlying true redshift histograms of the simulated galaxies as calibrated estimates of the KiDS-1000 tomographic $n(z)$.

3.1. Galaxy population model

Our analysis is based on the *pop-cosmos* generative model for the redshift-evolving galaxy population (J. Alsing et al. 2024; S. Thorp et al. 2025). This is an SPS-based model, trained on deep ultraviolet (UV) to mid-infrared (MIR) photometry in 26 broad and narrow bands from the COSMOS2020 catalog (J. R. Weaver et al. 2022). The *pop-cosmos* training set consists of $\sim 420,000$ MIR-selected galaxies with Spitzer IRAC *Ch. 1* < 26 . The SPS parametrization in *pop-cosmos* is based on a variant of the Prospector- α model (J. Leja

Table 1. The SPS and other parameters used in the `pop-cosmos` galaxy population model.

| symbol / unit | definition |
|------------------------------------------------|----------------------------------------|
| $\log_{10}(M_{\star}^{\text{form}}/M_{\odot})$ | logarithm of stellar mass formed |
| $\log_{10}(Z_{\star}/Z_{\odot})$ | logarithm of stellar metallicity |
| $\Delta \log_{10}(\text{SFR})_{\{2:7\}}$ | SFR ratios between SFH bins |
| τ_2/mag | diffuse dust optical depth |
| n | index for diffuse dust attenuation law |
| τ_1/τ_2 | birth cloud dust optical depth |
| $\ln(f_{\text{AGN}})$ | logarithm of AGN luminosity fraction |
| $\ln(\tau_{\text{AGN}})$ | logarithm of AGN torus optical depth |
| $\log_{10}(Z_{\text{gas}}/Z_{\odot})$ | logarithm of gas-phase metallicity |
| $\log_{10}(U_{\text{gas}})$ | logarithm of gas ionization |
| z | redshift |

et al. 2017, 2018, 2019b,a), providing a 16-parameter representation of each galaxy. The model uses: a non-parametric star formation history (SFH; J. Leja et al. 2019a), represented by 6 parameters; a two-component dust attenuation model (S. Charlot & S. M. Fall 2000), including a birth-cloud (affecting stars younger than 10 Myr) and diffuse (affecting all stars) component; a variable attenuation law slope and associated UV bump strength (D. Calzetti et al. 2000; S. Noll et al. 2009; M. Kriek & C. Conroy 2013); and an IR active galactic nucleus (AGN) contribution, associated with a clumpy dust torus (M. Nenkova et al. 2008a,b; J. Leja et al. 2018). The ionization parameter and gas-phase metallicity can vary independently from stellar metallicity, and nebular emission (lines and continuum) is based on the CLOUDY (G. J. Ferland et al. 2013) photoionization code (via model grids from N. Byler et al. 2017). The 16 SPS parameters used in `pop-cosmos` are listed in Table 1.

The SPS calculations in `pop-cosmos` are accelerated using the `Speculator` emulator (J. Alsing et al. 2020), a neural network model that is trained to reproduce the outputs of the Flexible Stellar Population Synthesis (FSPS; C. Conroy et al. 2009, 2010; C. Conroy & J. E. Gunn 2010) and Prospector (B. D. Johnson et al. 2021) libraries to better than $\sim 3\%$ precision in flux across 99.9% of allowable parameter space, and to better than $\sim 1\%$ precision across 99% of parameter space. For this work, we have trained emulators to predict FSPS/Prospector photometry for the KiDS passbands: the VST/OmegaCAM *ugri* bands and the VISTA/VIRCAM *ZYJHK_s* bands.

To describe the galaxy population, `pop-cosmos` defines a 16-dimensional probability distribution over the SPS parameters, represented using a score-based diffusion model (Y. Song et al. 2021). Mock galaxies can be generated by taking draws of SPS parameters

from the diffusion model, passing these through the `Speculator` emulator described above to generate noiseless photometry, incorporating recalibration terms for nebular emission and photometric zero points (using the formalism from B. Leistedt et al. 2023), and then applying a survey-specific data-model and selection effects to produce realistic noisy photometry for any survey with compatible selection effects (i.e., not deeper than the *Ch. 1* < 26 COSMOS2020 catalog used to train the model). The sections that follow will describe the construction of these models for KiDS, for rapid synthetic galaxy catalog generation (~ 1 million galaxies/GPU-hour).

As well as being used in a predictive capacity, the learned population distribution can be deployed as a prior over SPS parameters, to be used in SED fitting of individual galaxies’ photometry. This provides additional leverage over less-informative broader priors (e.g., J. Leja et al. 2017), and offers a data-driven alternative to priors based on empirical scaling relations (e.g., B. Wang et al. 2023). S. Thorp et al. (2024, 2025) demonstrated that when used as a data-driven prior in this way, `pop-cosmos` yields more accurate individual photometric redshifts than conventional SED fitting algorithms such as LePhare (S. Arnouts et al. 1999; O. Ilbert et al. 2006, 2009) and EAZY (G. B. Brammer et al. 2008). In H26 a similar demonstration will be provided for redshifts derived from *ugriZYJHK_s* photometry of the KiDS-1000 galaxies with `pop-cosmos`, demonstrating the ability to go from the 26-band setting of S. Thorp et al. (2024) to 9 bands. In this work, we will be demonstrating `pop-cosmos` as a tool for estimating population-level redshift distributions.

The population model presented in S. Thorp et al. (2025) is ideal for the task of estimating KiDS redshift distributions. The *Ch. 1* < 26 COSMOS2020 training sample has a high degree of completeness at the KiDS limiting magnitude (based on COSMOS2020 data, we estimate that $\sim 96\%$ of galaxies with $r < 25$ would be included in an *Ch. 1* < 26 selection). With appropriate selection applied, we therefore expect synthetic galaxies drawn from `pop-cosmos` to be representative of the galaxy population probed by KiDS. The first step to generate our KiDS-like mock catalogs is to repeatedly draw SPS parameters and redshifts from the `pop-cosmos` model, which are then passed through our KiDS SPS emulator to obtain noiseless model fluxes, $\mathbf{F} = (F_u, F_g, \dots, F_{K_s})$, in the *ugriZYJHK_s* bands.

3.2. Data model

Taking our large sample of mock galaxies with noiseless model fluxes as an input, we construct a data model for the measurement noise and selection criteria which combine to generate the KiDS catalogs (Section 2.1). Conceptually, the natural sequence for a given galaxy would be to i) start with the depth or noise level in each band, ii) add photometric noise to the noiseless model

fluxes to obtain measured fluxes, and then iii) apply the selection criteria. We cannot do this, however, as the pre-existing SKiLLS image simulations (S.-S. Li et al. 2023a) from which we learn these distributions include photometric measurements only for detected sources. For this reason, we factorize the data model to use distributions conditioned on detection from the outset, without any loss of generality¹⁸.

The quantities used in our KiDS data model, defined in Table 2, include both fluxes (most natural for the statistical formalism) and magnitudes (used for learning the relevant distributions). The r band is singled out as the KiDS detection band; quantities in the other bands only need to be considered for detected sources. We characterise the depth of the images using the reported limiting magnitudes, which in KiDS are equivalent to the 1-sigma uncertainty¹⁹ on the 9 GAaP fluxes, σ_{GAaP} . Additionally, the uncertainty on the AUTO flux, $\sigma_{r_{\text{AUTO}}}$, must also be modeled, because it differs from $\sigma_{r_{\text{GAaP}}}$ given the different type of flux (Section 2.1). For a galaxy with noiseless model fluxes \mathbf{F} observed with GAaP uncertainties σ_{GAaP} our data model is then defined by $p(\hat{F}_{\text{AUTO}}, \hat{\mathbf{F}}_{\text{GAaP}}, \sigma_{r_{\text{AUTO}}}, \text{det} | \sigma_{\text{GAaP}}, \mathbf{F})$, the joint distribution over detection, det, measured r -band AUTO flux, \hat{F}_{AUTO} and the measured GAaP fluxes. We then factor this full distribution as

$$\begin{aligned}
 & p\left(\hat{F}_{\text{AUTO}}, \hat{\mathbf{F}}_{\text{GAaP}}, \sigma_{r_{\text{AUTO}}}, \text{det} \mid \sigma_{\text{GAaP}}, \mathbf{F}\right) = \\
 & \underbrace{p\left(\text{det} \mid \sigma_{\text{GAaP}}, \mathbf{F}\right)}_{\text{detection}} \times \underbrace{p\left(\sigma_{r_{\text{AUTO}}} \mid \sigma_{\text{GAaP}}, \mathbf{F}, \text{det}\right)}_{\text{uncertainty}} \\
 & \times \underbrace{p\left(\hat{F}_{\text{AUTO}}, \hat{\mathbf{F}}_{\text{GAaP}} \mid \sigma_{r_{\text{AUTO}}}, \sigma_{\text{GAaP}}, \mathbf{F}, \text{det}\right)}_{\text{noise}}, \quad (3)
 \end{aligned}$$

where the first term is the detection model (Section 3.2.1) and the second and third terms, which correspond to the uncertainty model (Section 3.2.2) and the noise model (Section 3.2.3), are both conditioned

¹⁸ In J. Alsing et al. (2024) and S. Thorp et al. (2025) we were able to avoid the complication of having to define a data model conditioned on detection as we used selection cuts of $r < 25$ and $Ch. 1 < 26$, respectively.

¹⁹ Throughout this work, limiting magnitudes refer to 1σ GAaP flux uncertainties rather than the 5σ detection thresholds more commonly adopted in optical surveys. This convention is natural for GAaP photometry, where aperture-matched flux uncertainties directly characterize measurement precision. We note an important distinction: while survey depth at a given position can be characterized by a limiting magnitude (determined by sky background, exposure time, and seeing), individual source flux uncertainties only approach this depth-based limit for faint sources in the background-dominated regime (S. B. Howell 2006). Brighter sources have additional uncertainty contributions from source photon statistics. This is particularly relevant for our data model, where we condition on both noiseless source fluxes and position-dependent depth, assuming background-limited uncertainties.

Table 2. Symbol definitions for the data model. All magnitudes and fluxes are extinction- and aperture-corrected as described in the text. The first block lists quantities for a single band (shown for the r -band); the same notation applies to other bands by substituting the band name. The second block lists multi-band model quantities and derived indicators.

| symbol | definition |
|----------------------------------|-------------------------------------------------------------------------------------------|
| r | r -band model (noiseless, FSPS) magnitude |
| $\sigma_{r_{\text{GAaP}}}$ | GAaP r -band 1-sigma flux uncertainty |
| $r_{\text{GAaP}, 1\sigma}$ | $\sigma_{r_{\text{GAaP}}}$ as an AB magnitude (magnitude limit) |
| \hat{r}_{GAaP} | GAaP r -band measured magnitude |
| $\hat{F}_{r_{\text{GAaP}}}$ | GAaP r -band measured flux |
| r_{AUTO} | AUTO r -band measured magnitude |
| $\sigma_{r_{\text{AUTO}}}$ | AUTO r -band 1-sigma flux uncertainty |
| $r_{\text{AUTO}, 1\sigma}$ | $\sigma_{r_{\text{AUTO}}}$ as an AB magnitude |
| $\hat{F}_{r_{\text{AUTO}}}$ | AUTO r -band measured flux |
| det | Detection boolean indicator |
| \mathbf{F} | <i>ugriZYJHK_s</i> FSPS model fluxes |
| $\hat{\mathbf{F}}_{\text{AUTO}}$ | r -band AUTO measured flux |
| $\hat{\mathbf{F}}_{\text{GAaP}}$ | <i>ugriZYJHK_s</i> GAaP noisy fluxes |
| σ_{GAaP} | <i>ugriZYJHK_s</i> GAaP flux uncertainties (equivalent to the magnitude limits) |

on detection and so can be learned from the SKiLLS simulations.

3.2.1. Detection model

The KiDS catalogues are selected based on r -band images, so the detection probability, written in generality as $p(\text{det} | \sigma_{\text{GAaP}}, \mathbf{F})$ in Equation 3, can be written more simply as $p(\text{det} | \sigma_{\text{GAaP}}, r)$, where the switch from flux to magnitude makes fitting easier. The difficulty here is that the actual detection method is not a simple magnitude/flux cut, but depends on factors inherent to the images, such as the number of connected pixels with values above a detection threshold.

We use a random forest classifier (L. Breiman 2001; F. Pedregosa et al. 2011) to represent $p(\text{det} | \sigma_{\text{GAaP}}, r)$, training it on 800,000 objects randomly sampled from SKiLLS truth input catalog. For detected objects the inputs are the reported r -band magnitude and magnitude limit, while for undetected objects we assign magnitude limits drawn from the rest of the catalog.

We also need to ensure that the distributions of sampled r magnitudes and the magnitude limits match the equivalent distributions in the KiDS data. We implement this with a rejection sampling strategy. We model the target distribution (obtained using the SKiLLS sam-

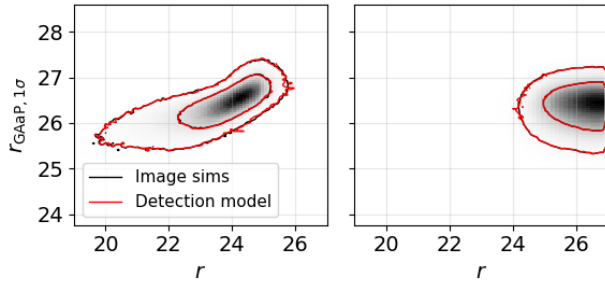


Figure 1. Validation of the r -band detection model: probability density of the GAaP magnitude limit given the noiseless model magnitude, for detected (left) and undetected (right) objects, for the SKiLLS simulations (black) and our model (red, described in Section 3.2.1). The contours enclose 68% and 95% of the total probability.

ple) with a second random forest, also trained on 800,000 sources.

Figure 1 shows a numerical validation of this two-step detection model, confirming that our model reproduces these distributions well.

3.2.2. Uncertainty model

In KiDS the reported GAaP magnitude limits, corresponding to a GAaP flux of 1σ , are a reasonable proxy for the depth and so do not need to be included in the data model. However, this is not the case for the Kron-like AUTO magnitude, and its error $\sigma_{r_{\text{AUTO}}}$, which sensitive to galaxy morphology (light profile, size, Sérsic index) and local conditions (PSF, neighboring sources). Since pop-cosmos does not provide a generative model for images, we need to use the SKiLLS image simulations learn the distribution $p(\sigma_{r_{\text{AUTO}}} | \sigma_{\text{GAaP}}, \mathbf{F}, \text{det})$ introduced in Equation 3.

To learn $p(\sigma_{r_{\text{AUTO}}} | \sigma_{\text{GAaP}}, \mathbf{F}, \text{det})$ we use a conditional ODE flow (Y. Lipman et al. 2023) trained with flow-matching²⁰ on 800,000 training samples from SKiLLS, as detailed in Section A.2. As illustrated in Figure 2 this model is able to accurately reproduce the details of this distribution.

3.2.3. Noise model

Measured fluxes differ from true fluxes for several distinct reasons; these are jointly referred to as (photometric) noise, defined here by the distribution $p(\hat{F}_{\text{AUTO}}, \hat{F}_{\text{GAaP}} | \sigma_{r_{\text{AUTO}}}, \sigma_{\text{GAaP}}, \mathbf{F}, \text{det})$, as introduced in Equation 3. It is convenient to work in terms of residuals, i.e. the difference between the observed and model fluxes, divided by the uncertainty. In principle, such residuals should be exactly uncorrelated if background

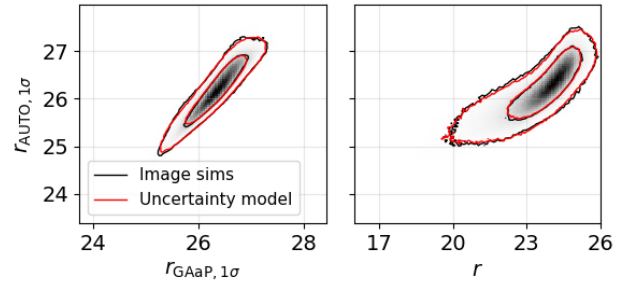


Figure 2. Validation of the r -band uncertainty model: probability density of the AUTO flux uncertainty (vertical axes, converted to AB magnitude) as a function of the magnitude corresponding to a flux of $\sigma_{r_{\text{GAaP}}}$ (left) and the noiseless model magnitude (right), for the SKiLLS simulations (black) and our model (red, described in Section 3.2.2). The contours enclose 68% and 95% of the total probability.

subtraction uncertainties dominate and the time interval between the measurements being made is sufficiently long, as is the case here. For ideal flux measurement and depth characterization pipelines, one would also expect these residuals to be nearly zero-mean, unit-variance Gaussian distributed, and independent of depth or input magnitudes. In practice, heavy tails and magnitude-dependent trends (and non-Gaussianity more generally) in these distributions are not only unavoidable, but are prevalent for the faint galaxies entering the KiDS-1000 sample. For example, galaxies near the detection limit show asymmetric errors with negative flux measurements, and faint extended sources exhibit systematically underestimated fluxes. These non-Gaussian features arise from source blending, background subtraction uncertainties, and the discrete pixel nature of images. Neglecting them would create discrepancies between the data and our simulated samples, and in turn, in the estimated redshift distributions.

For these reasons, we model the 10-dimensional flux noise residuals with another conditional ODE flow. The training data consists of 100 random tiles from SKiLLS (S.-S. Li et al. 2023a), each residual being calculated as the difference between the reported flux measurement (AUTO or GAaP) and the noiseless flux model (originally from the ProSpect SPS model; A. S. G. Robotham et al. 2020) divided by the reported flux uncertainty. We also condition on the 9-band noiseless magnitudes. Details of the training and model architecture are provided in Section A.3.

Figure 3 shows the resulting model, compared with the input data, demonstrating satisfactory agreement. We found that alternative models such as normalizing flows or correlated Student’s t distributions did not perform well, especially struggling to perform simultaneously well at the bright and the faint ends of the flux noise residuals.

²⁰ Our implementation, flowfusion, is publicly available at <https://github.com/Cosmo-Pop/flowfusion>.

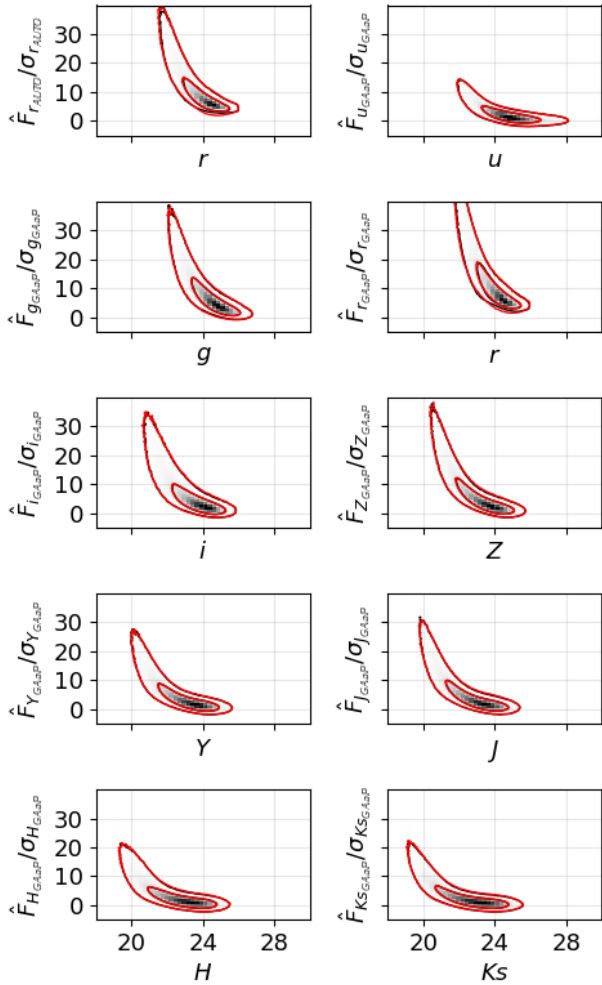


Figure 3. Validation of the noise model: probability density of the flux signal-to-noise ratio as a function of the noiseless model magnitude in each band, for the SKiLLS simulations (black) and our model (red, described in Section 3.2.3). Contours enclose 68% and 95% of the joint probability density.

3.3. Tomographic binning

For cosmological analyses, the detected galaxies are commonly sorted into tomographic redshift bins. This separation can be achieved with any method, but the choice affects the constraining power and residual systematic biases (e.g., which redshift bin is more likely to capture the stars misclassified as galaxies, and how much this depends on the multi-band photometric noise). In KiDS, photometric redshift estimates are based on BPZ (N. Benítez 2000). A posterior distribution is obtained by first evaluating a likelihood taking in the flux and flux uncertainties available, as a function of three parameters: redshift, absolute magnitude, and index of the galaxy SED template considered. Second, a prior (a simple parametric function of redshift) is incorporated. BPZ then marginalizes over the absolute magnitude and

the choice of SED template, in order to deliver a posterior probability distribution on redshift alone. The final estimated photometric redshift value, Z_B , is the maximum a posteriori (MAP) value, and in KiDS it is used to sort galaxies into redshift bins. To keep as close to the KiDS team’s analysis configuration as possible, we employ the BPZ configuration taken from the DR5 analysis (A. H. Wright et al. 2024) because we were unable to exactly reproduce the publicly released DR4 BPZ redshifts using the settings recommended in the KiDS analysis (K. Kuijken et al. 2019). This could be due to untracked changes in configuration or input files. The median and 95th-percentile of absolute differences in Z_B between the two configurations are 0.01 and 0.69, respectively, indicating that differences are only significant for a small fraction of the catalog. However, quantifying the net impact on $n(z)$ would require running our full forward-modeling pipeline with both setups, which was not possible. Because we use the DR5 BPZ configuration whereas the published KiDS-1000 $n(z)$ were derived with the DR4 setup, our tomographic samples are not strictly identical across the source sample, and differences between the two sets of $n(z)$ should be interpreted with this in mind.

3.4. KiDS-1000 selection

The KiDS-1000 cosmic shear sample (B. Giblin et al. 2021) is a curated subset of the full KiDS DR4 catalog, optimized for weak lensing measurements through multiple quality criteria including detection significance thresholds, star-galaxy separation, shape measurement quality flags from *lensfit*, and removal of sources near bright stars or survey boundaries (B. Giblin et al. 2021). As explained in Section 2, we obtain the KiDS-1000 binary flag by cross-matching the DR4 data with the publicly released KiDS-1000 catalog, since the flag cannot be reproduced from the information available in the DR4 catalogs. Thus, we implement a machine learning approach that emulates the KiDS-1000 selection: a random forest classifier that distinguishes between galaxies included in KiDS-1000 versus those in the parent DR4 catalog. When doing inference, rather than applying a deterministic classification threshold, the predicted class is drawn from a Bernoulli distribution with probability equal to the predicted class probability given by the random forest. Details of training and architecture are provided in Section A.4. The classifier operates on 20 photometric features: AUTO magnitude, GAaP magnitudes in all 9 bands (*ugriZYJHK_s*), and limiting magnitudes derived from the $1-\sigma$ flux uncertainties.

The trained random forest classifier provides a practical approximation of the KiDS-1000 selection function. On the test set it reaches an overall accuracy of $\sim 63\%$ in a highly imbalanced regime where only $\sim 25\text{--}30\%$ of DR4 galaxies belong to KiDS-1000. A trivial classifier that labels all objects as non-KiDS-1000 would already achieve $\sim 70\%$ accuracy but zero recall; our performance

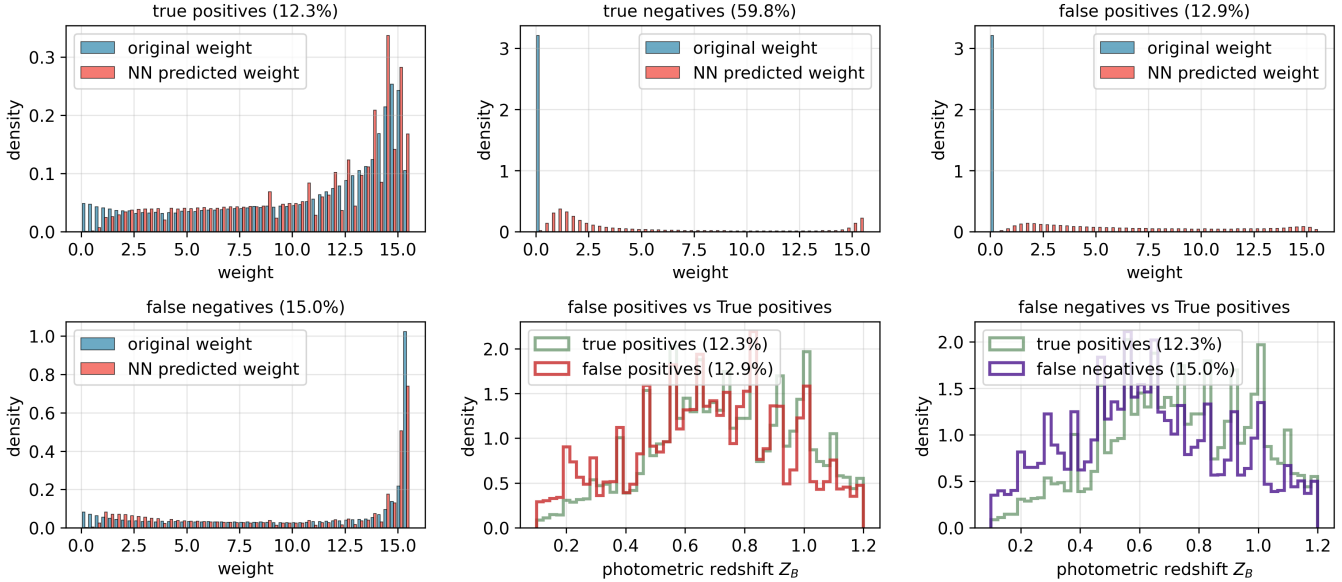


Figure 4. Performance of the classifier predicting the KiDS-1000 class, as a function of the *lensfit* weight (true and predicted with the regressor presented in Section 3.5) and the photometric redshift. True positives show higher *lensfit* weights (left panel), confirming the classifier identifies high-quality sources. False positives cluster at low weights and high BPZ photometric redshifts Z_B , indicating contamination from low-quality measurements at the survey edges.

therefore reflects a non-trivial compromise between recovering KiDS-1000 sources and limiting contamination. More informatively, the Receiver Operating Characteristic (ROC) curve, which plots the true positive rate against the false positive rate as the decision threshold is varied, has an area under the curve of $\simeq 0.90$. This quantifies the probability that the classifier assigns a higher score to a randomly chosen positive example than to a randomly chosen negative example, indicating strong intrinsic discrimination. At our fiducial operating point (defined by binomial sampling from the classifier’s raw probability predictions) the classifier attains a precision of ~ 0.44 and a recall of ~ 0.46 for the KiDS-1000 class; alternative thresholds could increase recall at the expense of purity.

Feature-importance analysis shows that the Z - and i -band GAaP magnitudes dominate, followed by the r -band and near-infrared GAaP magnitudes and the limiting magnitudes. The classifier maintains an accuracy close to the global value across well-populated magnitude bins, with best performance around $r_{\text{AUTO}} \simeq 21\text{--}23$, near the peak of the KiDS-1000 number counts.

Figure 4 further examines classifier behaviour and includes the weight predictions described in the next section. The weight distributions for galaxies classified as KiDS-1000 members show the expected bimodal *lensfit* structure, with true positives having systematically higher weights than false positives, confirming that the classifier preferentially selects galaxies with better shape-measurement quality. At the ensemble level, the redshift distributions of selected galaxies closely match those of the true KiDS-1000 sample in all tomographic

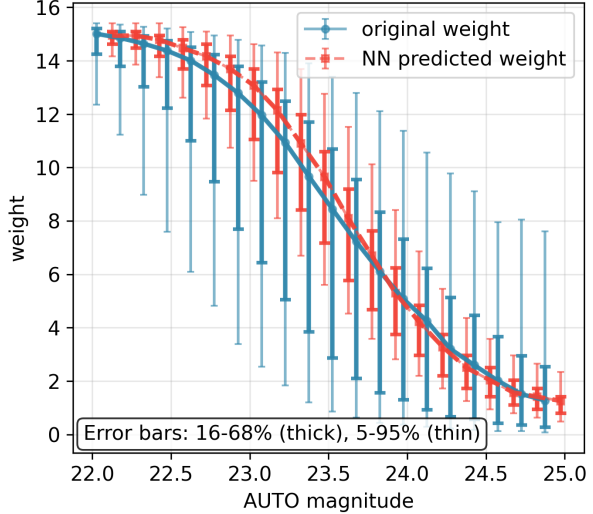


Figure 5. Performance of the neural network regressor for *lensfit* weight prediction. Mean predicted weights (red) versus true weights (blue) as a function of AUTO magnitude, showing good agreement despite underestimated scatter.

bins, with differences in the mean redshift below the level relevant for our cosmological analysis.

3.5. *lensfit* weight prediction

The *lensfit* weights provide a quantitative measure of shape-measurement quality for weak lensing analyses (L. Miller et al. 2013): they are inversely related to the variance of the shear estimates, so galaxies with better-constrained shapes receive higher weights and

contribute more reliably to the cosmic shear signal (B. Giblin et al. 2021). We implement a neural network regressor to predict *lensfit* weights, from the same 20 photometric features as above. Details of training and architecture are provided in Section A.5. Training data is restricted to KiDS-1000 galaxies only. The trained neural network achieves good performance in predicting *lensfit* weights. On the KiDS-1000 test sample the model attains a mean absolute error of 2.30, a root mean squared error of 3.25, and an R^2 score of 0.58. This level of scatter is consistent with the fact that *lensfit* weights depend on quantities that are not available in the catalog photometry, such as detailed galaxy morphology, local PSF quality, and proximity to bright stars.

As shown in Figure 5, the performance varies with magnitude. The model successfully reproduces the expected trend of decreasing weight with increasing r_{AUTO} and accurately captures the mean weight as a function of magnitude, with a typical bias of only ~ 0.5 . The observed scatter in the true data is roughly twice as large as the model-predicted scatter, reflecting the missing non-photometric information, but this has negligible impact on the redshift distributions relevant for our analysis. The network recovers the overall shape of the weight distribution and performs particularly well in the critical high-weight range of 10–15. The residuals are approximately symmetric, with a mean of -0.14 and a standard deviation of 3.25, indicating well-behaved errors without strong systematic trends.

4. RESULTS

We now describe the synthetic KiDS DR4 and KiDS-1000 galaxy catalogs, obtained by drawing galaxies from one of the population models (**shark** or **pop-cosmos**), and applying the data model (see Section 3.2). Finally, the KiDS-1000 selection (see Section 3.4) and tomographic binning (see Section 3.3) steps are applied in order to obtain mock galaxy samples in tomographic redshift bins. *lensfit* weights are derived with our emulator (see Section 3.5).

4.1. SKiLLS footprint

Figure 6 shows the predicted redshift distributions of galaxies obtained by simulating the KiDS-1000 tomographic samples with the **shark** and **pop-cosmos** population models, both interfaced with our data model. Galaxies are injected at the depths (magnitude limits in the 9 bands) of objects from the SKiLLS footprint, so that the resulting galaxy samples have the same observing conditions as SKiLLS.

First and foremost, this figure serves as a validation of our data model (Section 3.2): the redshift distributions obtained by combining **shark** galaxies with our data model (light blue) are essentially identical to the ‘true’ distributions from SKiLLS (dark blue). The differences between the means of the redshift distributions are all < 0.005 , which is well within requirements for

ongoing weak lensing surveys. Given the large number of galaxies in each tomographic bin, the statistical uncertainties on the inferred $n(z)$ are negligible.

Replacing **shark** for **pop-cosmos** mock galaxies (shown in red) results in more significant changes in the redshift distributions, with the largest shift in the highest-redshift bin ($\Delta z \sim 0.05\text{--}0.1$). This is the result of differences in the color–redshift relation between **shark**, shown in Figure 7, and **pop-cosmos**, shown in Figure 8: at high redshifts, **pop-cosmos** galaxies occupy a broader range of generally redder colors than **shark** (e.g. in $r - i$ and $i - Z$). As a result, BPZ more often assigns intermediate-redshift **pop-cosmos** galaxies to the highest bin and scatters some high-redshift objects to lower Z_B , whereas **shark** yields a simpler mapping of high-redshift colors into that bin. However, we cannot link these color differences to discrepancies in physical galaxy properties since no physical parameters are available for **shark**. These differences exemplify the contrasting philosophies of the two approaches: **pop-cosmos**’s data-driven approach directly learns the full diversity of observed color–redshift correlations, including population scatter; **shark**’s physics-based prescriptions produce more uniform color evolution that successfully matches aggregate properties such as luminosity functions and stellar masses, but not the detailed color–redshift distributions.

The ridges and bifurcations visible in the **pop-cosmos** color–redshift relation, particularly in the infrared bands, arise from strong nebular emission lines ($\text{H}\alpha$, $[\text{O III}]$, $\text{H}\beta$) transitioning across filter bandpasses. This likely reflects differences in emission line treatment: **pop-cosmos** includes more detailed nebular physics (B. Leistedt et al. 2023; S. Thorp et al. 2025), higher equivalent widths for star-forming galaxies, and greater diversity in star formation histories, while **shark**’s smoother tracks suggest weaker emission line contributions or simplified prescriptions. Star-forming galaxies with high specific star formation rates (sSFR) show the strongest features due to larger equivalent widths, while quiescent populations follow smoother continuum-dominated tracks. These differences in the color–redshift relation affect the $n(z)$ via the tomographic bin assignments, performed with BPZ Z_B ²¹.

4.2. KiDS DR4 data footprint

We now simulate galaxies at the depths of the real DR4 data, in order to span the same range of observing conditions. We pick 200 random tiles, which provides a sample representative of the DR4 data footprint. For each real KiDS-1000 object in these tiles, we draw from our model until a simulated object is accepted by our KiDS-1000 selection model. The resulting redshift dis-

²¹ Photo- z codes rely on capturing sharp color features to break degeneracies and assign accurate redshifts.

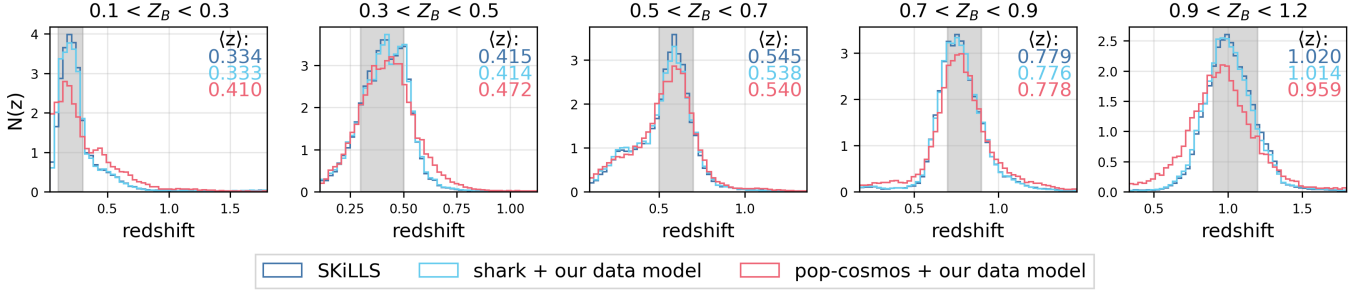


Figure 6. Redshift distributions in SKiLLS image simulations (dark blue), and from the *shark* (light blue) and *pop-cosmos* (red) population models processed through our data model, all with *lensfit* weights applied, shown in BPZ tomographic bins (titles). The grey band in each panel marks the BPZ Z_B range defining the bin. The distinct $n(z)$ recovered by *pop-cosmos* and *shark* are expected given the differences in their underlying modeled color-redshift relations (see text for details).

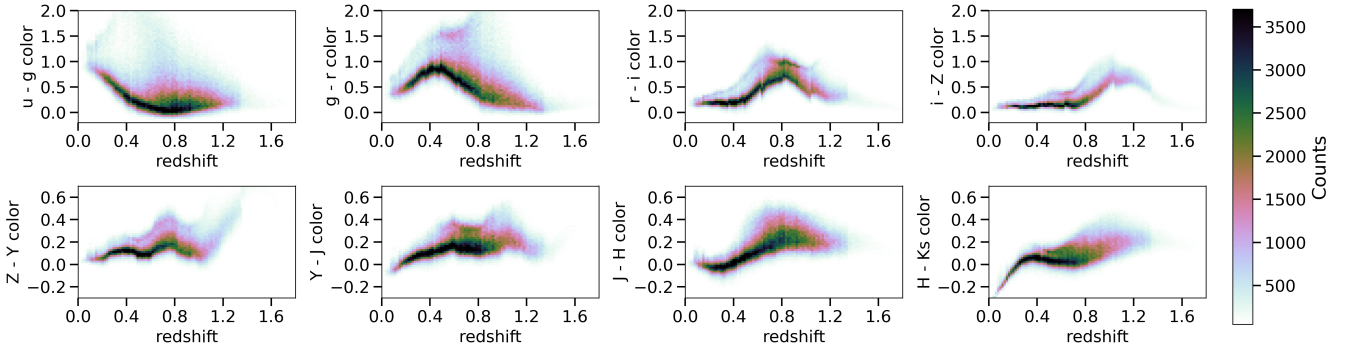


Figure 7. Noiseless color-redshift distributions for the *shark*-based mock KiDS-1000 sample in the SKiLLS footprint.

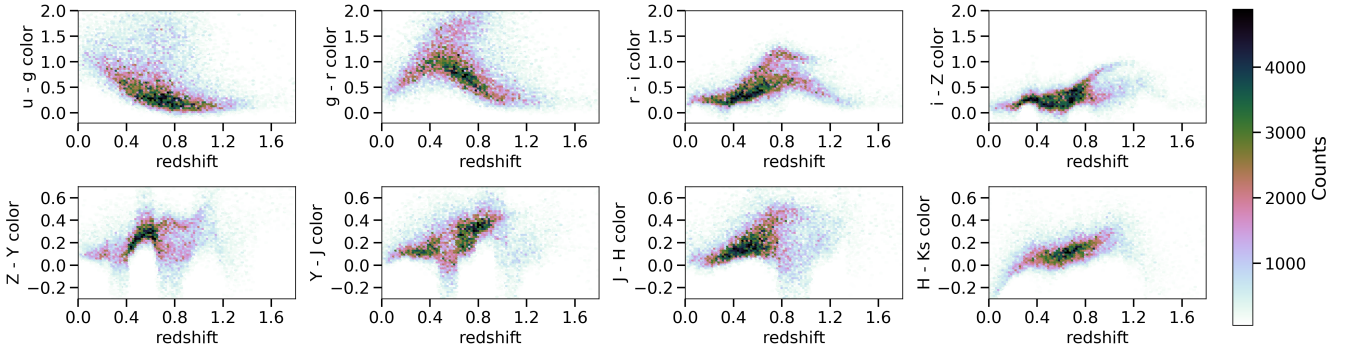


Figure 8. Noiseless color-redshift distributions for the *pop-cosmos*-based mock KiDS-1000 sample in the SKiLLS footprint.

distributions are shown in Figure 9. The differences with *shark* (not shown) are similar to those shown in Figure 6, which is expected since the depth distributions of KiDS DR4 and SKiLLS are so closely comparable.

We compare our results to the publicly released KiDS-1000 redshift distributions (H. Hildebrandt et al. 2021). These were obtained by re-weighting deep spectroscopic reference catalogues, including zCOSMOS (S. J. Lilly et al. 2007, 2009), VVDS-Deep (O. Le Fèvre et al. 2005, 2013, 2015), and DEEP2 (J. A. Newman et al. 2013), using a self-organizing map (SOM; T. Kohonen 1982; D. Masters et al. 2015) to match the nine-dimensional

magnitude-space of the source galaxies (A. H. Wright et al. 2020; H. Hildebrandt et al. 2021), with sources limited to a ‘gold’ selection that only includes regions of magnitude-space covered by the reference samples (A. H. Wright et al. 2020). In that framework, the accuracy of the calibration is limited by the depth, area and selection of the spectra, by cosmic variance in the calibration fields, and by the exclusion of sources in poorly sampled regions of color-magnitude space.

By contrast, our forward-modeling calibration is not tied to a particular spectroscopic training set. The differences between the publicly released redshift distribu-

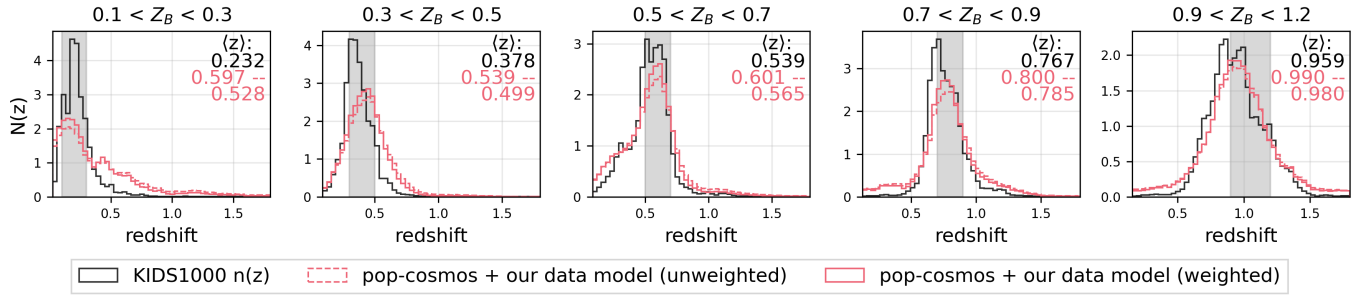


Figure 9. Redshift distributions in KiDS-1000 (black) and in the `pop-cosmos` population model processed through our data model. Solid red histograms include *lensfit* weights, while dashed red histograms are unweighted. The grey band in each panel marks the BPZ Z_B range defining the bin. There are inherent differences between the samples compared here (see text).

tions could be due to differences in the BPZ configuration between DR4 and DR5 (leading to differences in tomographic binning), or differences in the ‘gold’ selection, and, most importantly, from the fact that the spectroscopic reference sample used in the SOM approach does not necessarily span the same galaxy population as captured by the `pop-cosmos` model at KiDS depth. For reference, H. Hildebrandt et al. (2021) and A. H. Wright et al. (2025a) quote mean-redshift uncertainties of $\sigma_{\langle z \rangle} \simeq 0.01\text{--}0.05$ at 95% confidence per tomographic bin for the SOM-based calibration. As emphasized previously, the underlying galaxy samples compared in Figure 9 are somewhat different. Hence any systematic shifts in cosmological parameters between the two approaches can only be assessed in a full cosmological analysis, which we will present in an upcoming paper.

4.3. Galaxy populations in tomographic bins

The intrinsic properties of `pop-cosmos` galaxies in the simulated KiDS-1000 sample are illustrated in Figure 10. Each row shows a different physical parameter as a function of stellar mass (M_*/M_\odot): star formation rate (SFR); specific SFR (sSFR); stellar metallicity, Z_*/Z_\odot ; and diffuse dust optical depth, τ_2 . The first two rows highlight the star-forming main sequence, along which mass and SFR correlate closely (K. G. Noeske et al. 2007; E. Daddi et al. 2007; for a literature survey, see e.g. J. S. Speagle et al. 2014; P. Popesso et al. 2023), as well as the transition at high stellar mass between the star-forming and passive sequences (e.g. G. Kauffmann et al. 2003; I. K. Baldry et al. 2006; R. G. Bower et al. 2017). The third row probes the stellar mass–metallicity relation (e.g. A. Gallazzi et al. 2005, 2014; H. J. Zahid et al. 2017), whilst the fourth highlights the correlation between dust attenuation and stellar mass (e.g. T. Garn & P. N. Best 2010; H. J. Zahid et al. 2013, 2017).

The plotted quantities are the noiseless SPS parameters of the `pop-cosmos` galaxies that both pass the KiDS-1000 selection and are assigned to the corresponding tomographic bin based on their BPZ redshift. This reveals how the KiDS-1000 selection function and detection thresholds shape the distribution of intrinsic galaxy properties. At low redshift (first column), the

sample spans $10^7 \lesssim M_*/M_\odot \lesssim 10^{11}$, including both star-forming galaxies on the main sequence and massive quiescent systems (sSFR $\lesssim 10^{-11} \text{ yr}^{-1}$). The expected scaling relations emerge naturally: more massive galaxies are older, more metal-rich, and dustier, particularly on the star-forming sequence. With increasing redshift, the mass distribution shifts toward $M_* \gtrsim 10^{10} M_\odot$ due to the detection limit (effectively Malmquist bias), while the star-forming main sequence evolves to higher SFR and sSFR at fixed mass. In the higher redshift bins (fourth and fifth columns), clear bimodality appears between star-forming galaxies (sSFR $\simeq 10^{-9} \text{ yr}^{-1}$) and massive quiescent systems. At fixed mass, higher-redshift galaxies are younger, slightly less metal-rich, and show increased dust optical depth with both mass and SFR. These correlated trends in mass, SFR, metallicity, and dust shape the color–magnitude–redshift distribution that drives photometric redshift estimation and tomographic calibration.

It is instructive to compare Figure 10 with Figure 12 of H26, where similar relations between stellar mass and inferred physical properties are shown for the real KiDS-1000 galaxies, and with tomographic bins defined using `pop-cosmos`-based photometric redshifts rather than the BPZ Z_B . Qualitatively, the same structures are visible in both figures: a well-defined star-forming main sequence and a population of massive quenched galaxies in each tomographic bin, together with increasing characteristic stellar mass and sSFR toward higher redshift, and tightening mass–metallicity relations. However, H26 finds slightly sharper and more coherent sequences within each bin, with less leakage of low- or high-redshift populations across bin boundaries, while our BPZ-based bins display somewhat broader and more blended structures, especially at the edges of the tomographic ranges. This contrast is consistent with the higher redshift accuracy of `pop-cosmos` relative to BPZ, and it illustrates explicitly how improved photo- z performance tightens the mapping between physical properties and tomographic bin.

In addition to the relations between stellar mass and other properties, it is useful to examine how these

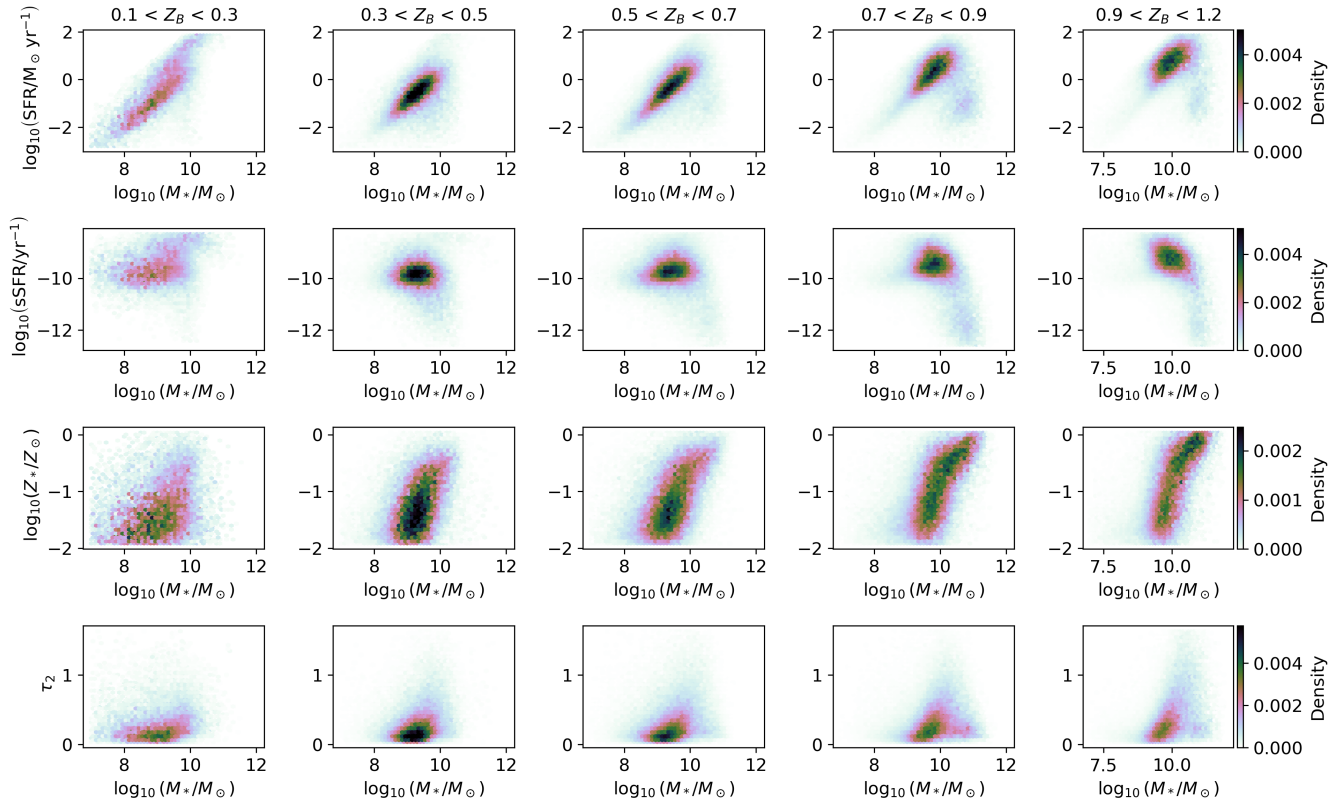


Figure 10. Stellar mass and other properties of *pop-cosmos* galaxies in the KiDS-1000 tomographic bins. Panels show the joint distribution of stellar mass with SFR (top row), sSFR (second row), stellar metallicity (third row), and diffuse dust optical depth (bottom row), for galaxies assigned to a given BPZ tomographic redshift bin (columns).

same populations populate color–redshift space. This is shown in Figure 11. These maps reveal the familiar sharp features associated with strong emission lines moving through the filters, as well as smooth trends whereby redder optical and NIR colors at fixed redshift correspond to higher mass, higher metallicities, larger dust optical depths, and lower sSFRs. Conversely, the bluest regions of each color–redshift relation are populated by low-mass, young, metal-poor galaxies with high specific star-formation rates. This can be compared directly to Figures 7–11 of H26, in which analogous color–redshift relations are plotted with the physical properties (including redshift) inferred from full SED fitting of individual KiDS-1000 galaxies. Qualitatively, the same structures are visible in both figures: the positions and shapes of the emission-line-induced breaks in color with redshift, the monotonic gradients of dust, metallicity and sSFR across the color–redshift plane, and the clear separation between star-forming and quenched populations. The main difference (causing the increased horizontal blurring of Figures. 7–11 of H26) is the result of the horizontal axis being the inferred photometric estimate as opposed to the true model redshift used here.

4.4. Number counts in tomographic bins

The numbers of galaxies in each tomographic bin can differ by $\sim 5\text{--}10\%$ between our mock catalogs and the SKiLLS image simulations or the KiDS data. The reasons for these differences are the changes in BPZ configuration outlined in Section 3.3, the differences in 9-band depths in the SKiLLS and DR4 data footprints, and the KiDS-1000 classifier employed. We isolated these effects and found that the tile-to-tile changes in 9-band depth combined with the choice of training data of the classifier is the most important effect. This is because the KiDS-1000 classifier effectively imposes a magnitude- and quality-dependent selection. Small tile-to-tile changes in limiting magnitudes shift the effective flux threshold, strongly affecting how many galaxies pass the cut near the survey flux limit. When the classifier is trained on SKiLLS or on the DR4 data, it sees different depth distributions and flag definitions, so it learns slightly different decision boundaries. Together, these effects change the selection efficiency and thus the number of galaxies in each tomographic bin, especially when training the classifier on the data and applying it to SKiLLS, or conversely. Nevertheless, we find that the shapes of the redshift distributions in tomographic bins are robust to these changes.

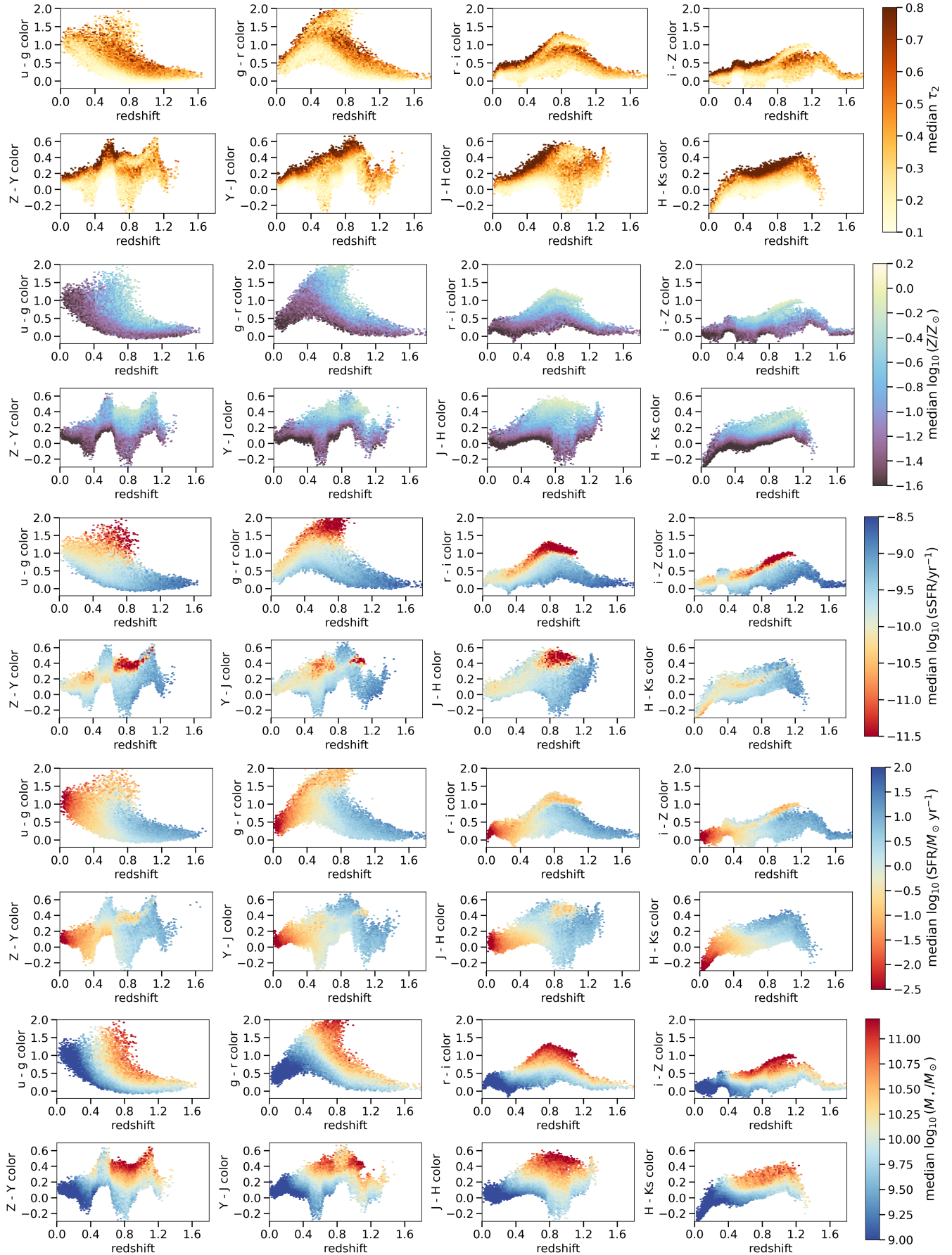


Figure 11. Noiseless color–redshift relations colored by physical properties of the pop-cosmos-based KiDS-1000 mocks.

5. DISCUSSION

The comparison between `shark` and `pop-cosmos` underscores the advantage of an empirically calibrated population model.

The `pop-cosmos` model has been extensively validated through several companion studies (J. Alsing et al. 2024; S. Thorp et al. 2024, 2025; S. Deger et al. 2025). These works demonstrate that it reproduces expected color–redshift relations and galaxy evolution trends, with per-galaxy photometric redshifts achieving scatter and outlier rates competitive with or better than other available methods (S. Thorp et al. 2024). In a companion paper (H26), the updated population model of S. Thorp et al. (2025) are applied to individual KiDS DR4 galaxies, yielding accurate photometric redshifts and physical property estimates for individual objects. Together, these studies establish `pop-cosmos` as empirically well-calibrated in the optical and NIR at KiDS depths.

`shark` provides a complementary perspective through its semi-analytic approach, which we use to probe systematic shifts under different galaxy-formation assumptions. Existing `shark` validation studies (C. d. P. Lagos et al. 2018, 2020; M. Bravo et al. 2020) have successfully tested predictions against luminosity functions across cosmic time, $z \simeq 0$ color distributions, submillimeter number counts, and color–color diagrams at $z \simeq 2$ –3. However, these validations focus on integrated properties and specific redshift slices rather than color evolution as a continuous function of redshift at $0.5 \lesssim z \lesssim 2$. Figure 7 of H26 reveals that the color bimodality at $z > 0.4$ due to the separation between the red sequence and the blue cloud is better reproduced by `pop-cosmos` (Figure 8) than `shark` (Figure 7). The systematic shifts we observe ($\Delta z \sim 0.05$ –0.1) when substituting them therefore highlight the sensitivity of forward-modeled redshift distributions to the calibration of the underlying population model.

The current implementation of our forward modeling framework presented here does, inevitably, have some limitations. However, our tests show no significant impact on $n(z)$ calibration or scientific conclusions. We now discuss these points in turn:

- The `pop-cosmos` model does not currently include galaxy morphological parameters (size, ellipticity, Sérsic index), which are known to correlate with photometric properties.

To investigate this correlation and any potential systematic shifts in the magnitude and color distributions, we have made tests with HSC-SSP data²² (H. Aihara et al. 2022), where KiDS-like flux and image-level cuts were applied to HSC shape catalogues. We find that such morphology- and resolution-dependent cuts mainly affect the

extreme tails of the color distributions and leave their bulk largely unchanged (Tudorache et al. in prep.). This demonstrates that the absence of explicit morphology in our forward modeling has a negligible impact on the color–redshift relation and hence on the tomographic $n(z)$ calibration.

- Our data model is trained exclusively on the SKiLLS image simulations, which have their own limitations.

The SKiLLS noise model uses a single-image approximation in the infrared bands, rather than fully simulating the VIKING paw-print observing strategy (A. Edge et al. 2013), and in the optical bands assumes Gaussian noise with empirically-calibrated variance. While these approximations produce realistic photometric scatter, they may not capture all subtleties of the noise properties, such as spatial correlations or non-Gaussian tails.

Additionally, the SKiLLS PSF modeling uses position-dependent polynomial reconstructions for the r -band and Moffat profiles for other bands (L. Miller et al. 2013), which may introduce small systematic differences compared to the actual survey PSFs.

These limitations are unlikely to significantly impact our redshift distribution estimates, as we condition our models on depth-dependent quantities and train on realistic detected galaxies. However, as surveys push toward higher precision on cosmological parameters, it will become essential to propagate residual sources of uncertainty in redshift calibration.

In principle, one could imagine calibrating $n(z)$ by combining the redshift posterior distributions from full SED inference on every source galaxy (B. Leistedt et al. 2016; A. I. Malz & D. W. Hogg 2022; M. Autenrieth et al. 2024). However, this is not practical for KiDS-1000: with only nine broad bands and many sources near the detection limits, individual-galaxy posteriors remain broad and sometimes multi-modal, even under the `pop-cosmos` prior (H26). This would propagate large per-object scatter into the $n(z)$. Moreover, such an approach would still need to model the full survey selection function. Our forward-modelling framework does this explicitly by propagating the population prior through the data model, making it a more robust route to $n(z)$ calibration.

After our DR4 data preparation pipeline was finalized KiDS Data Release 5 (A. H. Wright et al. 2024) was made available. Differences with DR4 include increased sky coverage, additional i -band observations, and improved astrometry, photometry, and redshift calibration (A. H. Wright et al. 2025a). However, the KiDS-1000 weak lensing catalog (B. Giblin et al. 2021; H. Hildebrandt et al. 2021) that we model in this work is a

²² The information to run such tests is not available for KiDS.

DR4 data product, with the equivalent DR5 weak lensing analysis having only been published very recently (A. H. Wright et al. 2025b).

6. CONCLUSIONS

We have developed a forward-modeling approach that infers galaxy redshift distributions directly from a generative galaxy population model combined with a realistic survey data model. Specifically, we combined the empirically calibrated `pop-cosmos` population model with a data model learned from KiDS image simulations (SKiLLS; S.-S. Li et al. 2023a) to forward-model the KiDS-1000 weak-lensing sample.

Our key findings are:

- **Data-model validation:** Machine learning models can accurately capture the complex transformations between intrinsic galaxy properties and observed photometry in KiDS, successfully reproducing the statistical properties of the SKiLLS synthetic galaxy catalogs when using `shark`, the galaxy population that was used to generate these simulations.
- **Importance of empirically calibrated population model:** Replacing `shark` by the `pop-cosmos` galaxy-population model leads to shifts of $\Delta z \simeq 0.05$ -0.1 in the first and last tomographic bins, demonstrating that population assumptions can substantially influence the predicted tomographic redshifts. These differences arise primarily from variations in the galaxy color-redshift relations near the tomographic bin boundaries, underscoring that careful empirical calibration of the galaxy population model is essential for robust redshift calibration.
- **Generalisation of `pop-cosmos` beyond its training data:** The forward-modeled KiDS-1000 redshift distributions obtained demonstrate that the COSMOS2020-trained `pop-cosmos` model can be applied successfully to a survey with different depth, selection, and observing conditions. This conclusion is further corroborated by the companion analysis H26, in which MCMC inference under the `pop-cosmos` prior is applied to KiDS-1000 galaxies cross-matched with DESI DR1 Bright Galaxy and Luminous Red Galaxy samples, yielding accurate photometric redshifts with low outlier fractions that satisfy Stage IV weak-lensing requirements.
- **Redshift distribution estimation:** The framework presented here represents a practical tool for estimating redshift distributions and quantifying systematic uncertainties. By combining the realism of data-driven population models with the efficiency of machine-learning-based observational

models, we can efficiently explore the impact of different assumptions about galaxy populations on cosmological measurements.

Building on the method developed here – and on the companion analysis of H26 – we plan to perform a full KiDS cosmological analysis using `pop-cosmos`-based redshift distributions. As Stage IV surveys push toward percent-level precision on cosmological parameters, such forward-modeling tools, grounded in empirically-calibrated population models such as `pop-cosmos` will be essential to ensure that systematic uncertainties in redshift calibration do not limit our ability to constrain fundamental physics.

DATA AVAILABILITY

We have used the gold sample of weak lensing and photometric redshift measurements from the fourth data release of KiDS (K. Kuijken et al. 2019; A. H. Wright et al. 2020; H. Hildebrandt et al. 2021; B. Giblin et al. 2021). Cosmological parameter constraints from KiDS-1000 have been presented in M. Asgari et al. (2021), C. Heymans et al. (2021) and T. Tröster et al. (2021), with the methodology presented in B. Joachimi et al. (2021). The SKiLLS simulations from S.-S. Li et al. (2023a) are available on `SurfDrive`²³, and are based on input galaxies from SURFS²⁴ (P. J. Elahi et al. 2018) and stars from TRILEGAL²⁵ (L. Girardi et al. 2005).

AUTHOR CONTRIBUTIONS

We outline the different contributions below using keywords based on the Contribution Roles Taxonomy (CRedit; A. Brand et al. 2015). **BL:** conceptualization; methodology; software; formal analysis; investigation; data curation; visualization; writing – original draft; writing – review & editing. **HVP:** conceptualization; methodology; visualization; investigation; validation; writing – review & editing; supervision; project administration; funding acquisition. **AH:** investigation; software; validation; visualization; writing – review & editing. **ST:** methodology; software; writing – review & editing. **DJM:** conceptualization; methodology; investigation; validation; writing – review & editing. **AL:** conceptualization; data curation; formal analysis; investigation; methodology; software; validation; visualization. **JA:** conceptualization; data curation; formal analysis; investigation; methodology; software; validation; visualization. **GJ:** software. **MNT:** investigation; validation; writing – review & editing; visualization. **SD:** investigation; writing – review & editing. **JL:** writing –

²³ <https://surfdrive.surf.nl/files/index.php/s/iSvDmHQJjDa0ewG>

²⁴ <https://surfdrive.surf.nl/files/index.php/s/uegK5tc15TbWib7>

²⁵ <https://surfdrive.surf.nl/files/index.php/s/dMsqnkeEUFSSLHE>

review & editing; validation. **BVdB**: validation; visualization. **AHW**: data curation; writing - review & editing. **SSL**: resources; writing - review & editing. **KK**: resources; writing - review & editing. **HH**: data curation; writing - review & editing.

ACKNOWLEDGEMENTS

BL is supported by the Royal Society through a University Research Fellowship. This work has been supported by funding from the European Research Council (ERC) under the European Union’s Horizon 2020 research and innovation programmes (grant agreement no. 101018897 CosmicExplorer). This work has been enabled by support from the research project grant ‘Understanding the Dynamic Universe’ funded by the Knut and Alice Wallenberg Foundation under Dnr KAW 2018.0067. HVP was additionally supported by the Göran Gustafsson Foundation for Research in Natural Sciences and Medicine. AHW is supported by the Deutsches Zentrum für Luft- und Raumfahrt (DLR), under project 50QE2305, made possible by the Bundesministerium für Wirtschaft und Klimaschutz, and acknowledges funding from the German Science Foundation DFG, via the Col-

laborative Research Center SFB1491 “Cosmic Interacting Matters - From Source to Signal”.

Facilities: Based on observations made with ESO Telescopes at the La Silla Paranal Observatory under programme IDs 177.A-3016, 177.A-3017, 177.A-3018 and 179.A-2004, and on data products produced by the KiDS consortium. The KiDS production team acknowledges support from: Deutsche Forschungsgemeinschaft, ERC, NOVA and NWO-M grants; Target; the University of Padova, and the University Federico II (Naples).

Software: **Astropy** (Astropy Collaboration et al. 2013, 2018, 2022), **NumPy** (C. R. Harris et al. 2020), **SciPy** (P. Virtanen et al. 2020), **Matplotlib** (J. D. Hunter 2007), **scikit-learn** (F. Pedregosa et al. 2011), **GALSim** (B. T. P. Rowe et al. 2015), **FSPS** (C. Conroy et al. 2009, 2010; C. Conroy & J. E. Gunn 2010), **Prospector** (B. D. Johnson et al. 2021), **CLOUDY** (G. J. Ferland et al. 2013), **Speculator** (J. Alsing et al. 2020), **pop-cosmos**²⁶ (J. Alsing et al. 2024; S. Thorp et al. 2025), **flowfusion**²⁷, **torchdiffeq** (R. T. Q. Chen et al. 2018), and the KiDS and SKILLS reduction pipelines (K. Kuijken et al. 2019; S.-S. Li et al. 2023a).

REFERENCES

- Aihara, H., AlSayyad, Y., Ando, M., et al. 2022, PASJ, 74, 247, doi: [10.1093/pasj/psab122](https://doi.org/10.1093/pasj/psab122)
- Aihara, H., Arimoto, N., Armstrong, R., et al. 2018, PASJ, 70, S4, doi: [10.1093/pasj/psx066](https://doi.org/10.1093/pasj/psx066)
- Alarcon, A., Hearin, A. P., Becker, M. R., et al. 2025, arXiv e-prints, arXiv:2510.27604, doi: [10.48550/arXiv.2510.27604](https://doi.org/10.48550/arXiv.2510.27604)
- Alarcon, A., Hearin, A. P., Becker, M. R., & Chaves-Montero, J. 2023, MNRAS, 518, 562, doi: [10.1093/mnras/stac3118](https://doi.org/10.1093/mnras/stac3118)
- Alsing, J., Peiris, H., Mortlock, D., Leja, J., & Leistedt, B. 2023, ApJS, 264, 29, doi: [10.3847/1538-4365/ac9583](https://doi.org/10.3847/1538-4365/ac9583)
- Alsing, J., Thorp, S., Deger, S., et al. 2024, ApJS, 274, 12, doi: [10.3847/1538-4365/ad5c69](https://doi.org/10.3847/1538-4365/ad5c69)
- Alsing, J., Peiris, H., Leja, J., et al. 2020, ApJS, 249, 5, doi: [10.3847/1538-4365/ab917f](https://doi.org/10.3847/1538-4365/ab917f)
- Arnaboldi, M., Capaccioli, M., Mancini, D., et al. 1998, The Messenger, 93, 30
- Arnouts, S., Cristiani, S., Moscardini, L., et al. 1999, MNRAS, 310, 540, doi: [10.1046/j.1365-8711.1999.02978.x](https://doi.org/10.1046/j.1365-8711.1999.02978.x)
- Asgari, M., Lin, C.-A., Joachimi, B., et al. 2021, A&A, 645, A104, doi: [10.1051/0004-6361/202039070](https://doi.org/10.1051/0004-6361/202039070)
- Astropy Collaboration, Robitaille, T. P., Tollerud, E. J., et al. 2013, A&A, 558, A33, doi: [10.1051/0004-6361/201322068](https://doi.org/10.1051/0004-6361/201322068)
- Astropy Collaboration, Price-Whelan, A. M., Sipőcz, B. M., et al. 2018, AJ, 156, 123, doi: [10.3847/1538-3881/aabc4f](https://doi.org/10.3847/1538-3881/aabc4f)
- Astropy Collaboration, Price-Whelan, A. M., Lim, P. L., et al. 2022, ApJ, 935, 167, doi: [10.3847/1538-4357/ac7c74](https://doi.org/10.3847/1538-4357/ac7c74)
- Autenrieth, M., Wright, A. H., Trotta, R., et al. 2024, MNRAS, 534, 3808, doi: [10.1093/mnras/stae2243](https://doi.org/10.1093/mnras/stae2243)
- Baldry, I. K., Balogh, M. L., Bower, R. G., et al. 2006, MNRAS, 373, 469, doi: [10.1111/j.1365-2966.2006.11081.x](https://doi.org/10.1111/j.1365-2966.2006.11081.x)
- Benítez, N. 2000, ApJ, 536, 571, doi: [10.1086/308947](https://doi.org/10.1086/308947)
- Bergé, J., Gamper, L., Réfrégier, A., & Amara, A. 2013, Astron. Comput., 1, 23, doi: [10.1016/j.ascom.2013.01.001](https://doi.org/10.1016/j.ascom.2013.01.001)
- Bertin, E., & Arnouts, S. 1996, A&AS, 117, 393, doi: [10.1051/aas:1996164](https://doi.org/10.1051/aas:1996164)
- Bower, R. G., Schaye, J., Frenk, C. S., et al. 2017, MNRAS, 465, 32, doi: [10.1093/mnras/stw2735](https://doi.org/10.1093/mnras/stw2735)
- Brammer, G. B., van Dokkum, P. G., & Coppi, P. 2008, ApJ, 686, 1503, doi: [10.1086/591786](https://doi.org/10.1086/591786)
- Brand, A., Allen, L., Altman, M., Hlava, M., & Scott, J. 2015, Learned Publishing, 28, 151, doi: [10.1087/20150211](https://doi.org/10.1087/20150211)
- Bravo, M., Lagos, C. d. P., Robotham, A. S. G., Bellstedt, S., & Obreschkow, D. 2020, MNRAS, 497, 3026, doi: [10.1093/mnras/staa2027](https://doi.org/10.1093/mnras/staa2027)

²⁶ <https://github.com/Cosmo-Pop/pop-cosmos>

²⁷ <https://github.com/Cosmo-Pop/flowfusion>

- Breiman, L. 2001, *Machine Learning*, 45, 5, doi: [10.1023/A:1010933404324](https://doi.org/10.1023/A:1010933404324)
- Byler, N., Dalcanton, J. J., Conroy, C., & Johnson, B. D. 2017, *ApJ*, 840, 44, doi: [10.3847/1538-4357/aa6c66](https://doi.org/10.3847/1538-4357/aa6c66)
- Calzetti, D., Armus, L., Bohlin, R. C., et al. 2000, *ApJ*, 533, 682, doi: [10.1086/308692](https://doi.org/10.1086/308692)
- Capaccioli, M., & Schipani, P. 2011, *The Messenger*, 146, 2
- Charlot, S., & Fall, S. M. 2000, *ApJ*, 539, 718, doi: [10.1086/309250](https://doi.org/10.1086/309250)
- Chen, R. T. Q., Rubanova, Y., Bettencourt, J., & Duvenaud, D. K. 2018, in *Advances in Neural Information Processing Systems 31*, ed. S. Bengio, H. Wallach, H. Larochelle, K. Grauman, N. Cesa-Bianchi, & R. Garnett, 6572–6583. <https://arxiv.org/abs/1806.07366>
- Colless, M., Dalton, G., Maddox, S., et al. 2001, *MNRAS*, 328, 1039, doi: [10.1046/j.1365-8711.2001.04902.x](https://doi.org/10.1046/j.1365-8711.2001.04902.x)
- Conroy, C. 2013, *ARA&A*, 51, 393, doi: [10.1146/annurev-astro-082812-141017](https://doi.org/10.1146/annurev-astro-082812-141017)
- Conroy, C., & Gunn, J. E. 2010, *ApJ*, 712, 833, doi: [10.1088/0004-637X/712/2/833](https://doi.org/10.1088/0004-637X/712/2/833)
- Conroy, C., Gunn, J. E., & White, M. 2009, *ApJ*, 699, 486, doi: [10.1088/0004-637X/699/1/486](https://doi.org/10.1088/0004-637X/699/1/486)
- Conroy, C., White, M., & Gunn, J. E. 2010, *ApJ*, 708, 58, doi: [10.1088/0004-637X/708/1/58](https://doi.org/10.1088/0004-637X/708/1/58)
- Czado, C. 2019, *Lecture Notes in Statistics*, Vol. 222, Analyzing dependent data with vine copulas (Cham: Springer), doi: [10.1007/978-3-030-13785-4](https://doi.org/10.1007/978-3-030-13785-4)
- Daddi, E., Dickinson, M., Morrison, G., et al. 2007, *ApJ*, 670, 156, doi: [10.1086/521818](https://doi.org/10.1086/521818)
- Dale, D. A., Helou, G., Magdis, G. E., et al. 2014, *ApJ*, 784, 83, doi: [10.1088/0004-637X/784/2/83](https://doi.org/10.1088/0004-637X/784/2/83)
- Dark Energy Survey Collaboration. 2005, arXiv e-prints, astro-ph/0510346, doi: [10.48550/arXiv.astro-ph/0510346](https://doi.org/10.48550/arXiv.astro-ph/0510346)
- Davidzon, I., Ilbert, O., Laigle, C., et al. 2017, *A&A*, 605, A70, doi: [10.1051/0004-6361/201730419](https://doi.org/10.1051/0004-6361/201730419)
- de Jong, J. T. A., Kuijken, K., Applegate, D., et al. 2013, *The Messenger*, 154, 44
- Deger, S., Peiris, H. V., Thorp, S., et al. 2025, arXiv e-prints, arXiv:2509.20430, doi: [10.48550/arXiv.2509.20430](https://doi.org/10.48550/arXiv.2509.20430)
- Driver, S. P., Norberg, P., Baldry, I. K., et al. 2009, *Astron. Geophys.*, 50, 5.12, doi: [10.1111/j.1468-4004.2009.50512.x](https://doi.org/10.1111/j.1468-4004.2009.50512.x)
- Edge, A., Sutherland, W., Kuijken, K., et al. 2013, *The Messenger*, 154, 32
- Elahi, P. J., Welker, C., Power, C., et al. 2018, *MNRAS*, 475, 5338, doi: [10.1093/mnras/sty061](https://doi.org/10.1093/mnras/sty061)
- Fenech Conti, I., Herbonnet, R., Hoekstra, H., et al. 2017, *MNRAS*, 467, 1627, doi: [10.1093/mnras/stx200](https://doi.org/10.1093/mnras/stx200)
- Ferland, G. J., Porter, R. L., van Hoof, P. A. M., et al. 2013, *RMxAA*, 49, 137, doi: [10.48550/arXiv.1302.4485](https://doi.org/10.48550/arXiv.1302.4485)
- Fischbacher, S., Kacprzak, T., Tortorelli, L., et al. 2025a, *JCAP*, 2025, 007, doi: [10.1088/1475-7516/2025/06/007](https://doi.org/10.1088/1475-7516/2025/06/007)
- Fischbacher, S., Moser, B., Kacprzak, T., et al. 2025b, *J. Open Source Software*, 10, 8766, doi: [10.21105/joss.08766](https://doi.org/10.21105/joss.08766)
- Fischbacher, S., Moser, B., Kacprzak, T., et al. 2025c, *J. Open Source Software*, 10, 8697, doi: [10.21105/joss.08697](https://doi.org/10.21105/joss.08697)
- Gallazzi, A., Bell, E. F., Zibetti, S., Brinchmann, J., & Kelson, D. D. 2014, *ApJ*, 788, 72, doi: [10.1088/0004-637X/788/1/72](https://doi.org/10.1088/0004-637X/788/1/72)
- Gallazzi, A., Charlot, S., Brinchmann, J., White, S. D. M., & Tremonti, C. A. 2005, *MNRAS*, 362, 41, doi: [10.1111/j.1365-2966.2005.09321.x](https://doi.org/10.1111/j.1365-2966.2005.09321.x)
- Garn, T., & Best, P. N. 2010, *MNRAS*, 409, 421, doi: [10.1111/j.1365-2966.2010.17321.x](https://doi.org/10.1111/j.1365-2966.2010.17321.x)
- Giblin, B., Heymans, C., Asgari, M., et al. 2021, *A&A*, 645, A105, doi: [10.1051/0004-6361/202038850](https://doi.org/10.1051/0004-6361/202038850)
- Girardi, L., Groenewegen, M. A. T., Hatziminaoglou, E., & da Costa, L. 2005, *A&A*, 436, 895, doi: [10.1051/0004-6361:20042352](https://doi.org/10.1051/0004-6361:20042352)
- Graham, A. W., & Driver, S. P. 2005, *PASA*, 22, 118–127, doi: [10.1071/AS05001](https://doi.org/10.1071/AS05001)
- Grathwohl, W., Chen, R. T. Q., Bettencourt, J., Sutskever, I., & Duvenaud, D. 2019, in *7th International Conference on Learning Representations*, ed. T. Sainath, New Orleans, LA, USA. <https://arxiv.org/abs/1810.01367>
- Griffith, R. L., Cooper, M. C., Newman, J. A., et al. 2012, *ApJS*, 200, 9, doi: [10.1088/0067-0049/200/1/9](https://doi.org/10.1088/0067-0049/200/1/9)
- Hahn, C., Kwon, K. J., Tojeiro, R., et al. 2023, *ApJ*, 945, 16, doi: [10.3847/1538-4357/ac8983](https://doi.org/10.3847/1538-4357/ac8983)
- Hahn, C., Aguilar, J. N., Alam, S., et al. 2024, *ApJ*, 963, 56, doi: [10.3847/1538-4357/ad19c8](https://doi.org/10.3847/1538-4357/ad19c8)
- Harris, C. R., Millman, K. J., van der Walt, S. J., et al. 2020, *Nature*, 585, 357, doi: [10.1038/s41586-020-2649-2](https://doi.org/10.1038/s41586-020-2649-2)
- Hearin, A. P., Chaves-Montero, J., Alarcon, A., Becker, M. R., & Benson, A. 2023, *MNRAS*, 521, 1741, doi: [10.1093/mnras/stad456](https://doi.org/10.1093/mnras/stad456)
- Herbel, J., Kacprzak, T., Amara, A., et al. 2017, *JCAP*, 2017, 035, doi: [10.1088/1475-7516/2017/08/035](https://doi.org/10.1088/1475-7516/2017/08/035)
- Heymans, C., Tröster, T., Asgari, M., et al. 2021, *A&A*, 646, A140, doi: [10.1051/0004-6361/202039063](https://doi.org/10.1051/0004-6361/202039063)
- Hildebrandt, H., van den Busch, J. L., Wright, A. H., et al. 2021, *A&A*, 647, A124, doi: [10.1051/0004-6361/202039018](https://doi.org/10.1051/0004-6361/202039018)
- Howell, S. B. 2006, *Handbook of CCD Astronomy*, 2nd edn., Cambridge Observing Handbooks for Research Astronomers (Cambridge, UK: Cambridge University Press), doi: [10.1017/CBO9780511807909](https://doi.org/10.1017/CBO9780511807909)

- Hunter, J. D. 2007, *Comput. Sci. Eng.*, 9, 90, doi: [10.1109/MCSE.2007.55](https://doi.org/10.1109/MCSE.2007.55)
- Ilbert, O., Arnouts, S., McCracken, H. J., et al. 2006, *A&A*, 457, 841, doi: [10.1051/0004-6361:20065138](https://doi.org/10.1051/0004-6361:20065138)
- Ilbert, O., Capak, P., Salvato, M., et al. 2009, *ApJ*, 690, 1236, doi: [10.1088/0004-637X/690/2/1236](https://doi.org/10.1088/0004-637X/690/2/1236)
- Iyer, K. G., Pacifici, C., Calistro-Rivera, G., & Lovell, C. C. 2026, in *Encyclopedia of Astrophysics*, ed. I. Mandel, Vol. 4 (Oxford: Elsevier), 236–281, doi: [10.1016/B978-0-443-21439-4.00127-9](https://doi.org/10.1016/B978-0-443-21439-4.00127-9)
- Joachimi, B., Lin, C. A., Asgari, M., et al. 2021, *A&A*, 646, A129, doi: [10.1051/0004-6361/202038831](https://doi.org/10.1051/0004-6361/202038831)
- Joe, H. 2014, *Monographs on Statistics and Applied Probability*, Vol. 134, Dependence modeling with copulas (New York: CRC Press), doi: [10.1201/b17116](https://doi.org/10.1201/b17116)
- Johnson, B. D., Leja, J., Conroy, C., & Speagle, J. S. 2021, *ApJS*, 254, 22, doi: [10.3847/1538-4365/abef67](https://doi.org/10.3847/1538-4365/abef67)
- Kannawadi, A., Hoekstra, H., Miller, L., et al. 2019, *A&A*, 624, A92, doi: [10.1051/0004-6361/201834819](https://doi.org/10.1051/0004-6361/201834819)
- Kauffmann, G., Heckman, T. M., White, S. D. M., et al. 2003, *MNRAS*, 341, 54, doi: [10.1046/j.1365-8711.2003.06292.x](https://doi.org/10.1046/j.1365-8711.2003.06292.x)
- Kingma, D. P., & Ba, J. 2015, in *3rd International Conference on Learning Representations*, ed. Y. Bengio & Y. LeCun, San Diego, CA, USA. <https://arxiv.org/abs/1412.6980>
- Kohonen, T. 1982, *Biological Cybernetics*, 43, 59, doi: [10.1007/BF00337288](https://doi.org/10.1007/BF00337288)
- Kriek, M., & Conroy, C. 2013, *ApJL*, 775, L16, doi: [10.1088/2041-8205/775/1/L16](https://doi.org/10.1088/2041-8205/775/1/L16)
- Kron, R. G. 1980, *ApJS*, 43, 305, doi: [10.1086/190669](https://doi.org/10.1086/190669)
- Kuijken, K. 2008, *A&A*, 482, 1053, doi: [10.1051/0004-6361:20066601](https://doi.org/10.1051/0004-6361:20066601)
- Kuijken, K. 2011, *The Messenger*, 146, 8
- Kuijken, K., Bender, R., Cappellaro, E., et al. 2002, *The Messenger*, 110, 15
- Kuijken, K., Heymans, C., Dvornik, A., et al. 2019, *A&A*, 625, A2, doi: [10.1051/0004-6361/201834918](https://doi.org/10.1051/0004-6361/201834918)
- Lagos, C. d. P., da Cunha, E., Robotham, A. S. G., et al. 2020, *MNRAS*, 499, 1948, doi: [10.1093/mnras/staa2861](https://doi.org/10.1093/mnras/staa2861)
- Lagos, C. d. P., Tobar, R. J., Robotham, A. S. G., et al. 2018, *MNRAS*, 481, 3573, doi: [10.1093/mnras/sty2440](https://doi.org/10.1093/mnras/sty2440)
- Le Fèvre, O., Vettolani, G., Garilli, B., et al. 2005, *A&A*, 439, 845, doi: [10.1051/0004-6361:20041960](https://doi.org/10.1051/0004-6361:20041960)
- Le Fèvre, O., Cassata, P., Cucciati, O., et al. 2013, *A&A*, 559, A14, doi: [10.1051/0004-6361/201322179](https://doi.org/10.1051/0004-6361/201322179)
- Le Fèvre, O., Tasca, L. A. M., Cassata, P., et al. 2015, *A&A*, 576, A79, doi: [10.1051/0004-6361/201423829](https://doi.org/10.1051/0004-6361/201423829)
- Leistedt, B., Alsing, J., Peiris, H., Mortlock, D., & Leja, J. 2023, *ApJS*, 264, 23, doi: [10.3847/1538-4365/ac9d99](https://doi.org/10.3847/1538-4365/ac9d99)
- Leistedt, B., Mortlock, D. J., & Peiris, H. V. 2016, *MNRAS*, 460, 4258, doi: [10.1093/mnras/stw1304](https://doi.org/10.1093/mnras/stw1304)
- Leja, J., Carnall, A. C., Johnson, B. D., Conroy, C., & Speagle, J. S. 2019a, *ApJ*, 876, 3, doi: [10.3847/1538-4357/ab133c](https://doi.org/10.3847/1538-4357/ab133c)
- Leja, J., Johnson, B. D., Conroy, C., & van Dokkum, P. 2018, *ApJ*, 854, 62, doi: [10.3847/1538-4357/aaa8db](https://doi.org/10.3847/1538-4357/aaa8db)
- Leja, J., Johnson, B. D., Conroy, C., van Dokkum, P. G., & Byler, N. 2017, *ApJ*, 837, 170, doi: [10.3847/1538-4357/aa5ffe](https://doi.org/10.3847/1538-4357/aa5ffe)
- Leja, J., Johnson, B. D., Conroy, C., et al. 2019b, *ApJ*, 877, 140, doi: [10.3847/1538-4357/ab1d5a](https://doi.org/10.3847/1538-4357/ab1d5a)
- Li, S.-S., Kuijken, K., Hoekstra, H., et al. 2023a, *A&A*, 670, A100, doi: [10.1051/0004-6361/202245210](https://doi.org/10.1051/0004-6361/202245210)
- Li, S.-S., Hoekstra, H., Kuijken, K., et al. 2023b, *A&A*, 679, A133, doi: [10.1051/0004-6361/202347236](https://doi.org/10.1051/0004-6361/202347236)
- Li, X., Miyatake, H., Luo, W., et al. 2022, *PASJ*, 74, 421, doi: [10.1093/pasj/psac006](https://doi.org/10.1093/pasj/psac006)
- Lilly, S. J., Le Fèvre, O., Renzini, A., et al. 2007, *ApJS*, 172, 70, doi: [10.1086/516589](https://doi.org/10.1086/516589)
- Lilly, S. J., Le Brun, V., Maier, C., et al. 2009, *ApJS*, 184, 218, doi: [10.1088/0067-0049/184/2/218](https://doi.org/10.1088/0067-0049/184/2/218)
- Lipman, Y., Chen, R. T. Q., Ben-Hamu, H., Nickel, M., & Le, M. 2023, in *11th International Conference on Learning Representations*, ed. Y. Liu, Kigali, Rwanda. <https://arxiv.org/abs/2210.02747>
- MacCrann, N., Becker, M. R., McCullough, J., et al. 2022, *MNRAS*, 509, 3371, doi: [10.1093/mnras/stab2870](https://doi.org/10.1093/mnras/stab2870)
- Malz, A. I., & Hogg, D. W. 2022, *ApJ*, 928, 127, doi: [10.3847/1538-4357/ac062f](https://doi.org/10.3847/1538-4357/ac062f)
- Mandelbaum, R. 2018, *ARA&A*, 56, 393, doi: [10.1146/annurev-astro-081817-051928](https://doi.org/10.1146/annurev-astro-081817-051928)
- Mandelbaum, R., Lanusse, F., Leauthaud, A., et al. 2018, *MNRAS*, 481, 3170, doi: [10.1093/mnras/sty2420](https://doi.org/10.1093/mnras/sty2420)
- Masters, D., Capak, P., Stern, D., et al. 2015, *ApJ*, 813, 53, doi: [10.1088/0004-637X/813/1/53](https://doi.org/10.1088/0004-637X/813/1/53)
- McFarland, J. P., Verdoes-Kleijn, G., Sikkema, G., et al. 2013, *Experimental Astronomy*, 35, 45, doi: [10.1007/s10686-011-9266-x](https://doi.org/10.1007/s10686-011-9266-x)
- Miller, L., Heymans, C., Kitching, T. D., et al. 2013, *MNRAS*, 429, 2858, doi: [10.1093/mnras/sts454](https://doi.org/10.1093/mnras/sts454)
- Moser, B., Kacprzak, T., Fischbacher, S., et al. 2024, *JCAP*, 2024, 049, doi: [10.1088/1475-7516/2024/05/049](https://doi.org/10.1088/1475-7516/2024/05/049)
- Nenkova, M., Sirocky, M. M., Ivezić, Ž., & Elitzur, M. 2008a, *ApJ*, 685, 147, doi: [10.1086/590482](https://doi.org/10.1086/590482)
- Nenkova, M., Sirocky, M. M., Nikutta, R., Ivezić, Ž., & Elitzur, M. 2008b, *ApJ*, 685, 160, doi: [10.1086/590483](https://doi.org/10.1086/590483)
- Newman, J. A., & Gruen, D. 2022, *ARA&A*, 60, 363, doi: [10.1146/annurev-astro-032122-014611](https://doi.org/10.1146/annurev-astro-032122-014611)

- Newman, J. A., Cooper, M. C., Davis, M., et al. 2013, *ApJS*, 208, 5, doi: [10.1088/0067-0049/208/1/5](https://doi.org/10.1088/0067-0049/208/1/5)
- Noeske, K. G., Faber, S. M., Weiner, B. J., et al. 2007, *ApJL*, 660, L47, doi: [10.1086/517927](https://doi.org/10.1086/517927)
- Noll, S., Pierini, D., Cimatti, A., et al. 2009, *A&A*, 499, 69, doi: [10.1051/0004-6361/200811526](https://doi.org/10.1051/0004-6361/200811526)
- Pedregosa, F., Varoquaux, G., Gramfort, A., et al. 2011, *J. Machine Learning Res.*, 12, 2825.
<http://jmlr.org/papers/v12/pedregosa11a.html>
- Planck Collaboration, Ade, P. A. R., Aghanim, N., et al. 2016, *A&A*, 594, A13, doi: [10.1051/0004-6361/201525830](https://doi.org/10.1051/0004-6361/201525830)
- Planck Collaboration, Aghanim, N., Akrami, Y., et al. 2020, *A&A*, 641, A6, doi: [10.1051/0004-6361/201833910](https://doi.org/10.1051/0004-6361/201833910)
- Popesso, P., Concas, A., Cresci, G., et al. 2023, *MNRAS*, 519, 1526, doi: [10.1093/mnras/stac3214](https://doi.org/10.1093/mnras/stac3214)
- Robotham, A. S. G., Bellstedt, S., Lagos, C. d. P., et al. 2020, *MNRAS*, 495, 905, doi: [10.1093/mnras/staa1116](https://doi.org/10.1093/mnras/staa1116)
- Rowe, B. T. P., Jarvis, M., Mandelbaum, R., et al. 2015, *Astron. Comput.*, 10, 121, doi: [10.1016/j.ascom.2015.02.002](https://doi.org/10.1016/j.ascom.2015.02.002)
- Schlafly, E. F., & Finkbeiner, D. P. 2011, *ApJ*, 737, 103, doi: [10.1088/0004-637X/737/2/103](https://doi.org/10.1088/0004-637X/737/2/103)
- Schlegel, D. J., Finkbeiner, D. P., & Davis, M. 1998, *ApJ*, 500, 525, doi: [10.1086/305772](https://doi.org/10.1086/305772)
- Scoville, N., Aussel, H., Brusa, M., et al. 2007, *ApJS*, 172, 1, doi: [10.1086/516585](https://doi.org/10.1086/516585)
- Song, Y., Sohl-Dickstein, J., Kingma, D. P., et al. 2021, in 9th International Conference on Learning Representations, ed. S. Mohamed.
<https://arxiv.org/abs/2011.13456>
- Speagle, J. S., Steinhardt, C. L., Capak, P. L., & Silverman, J. D. 2014, *ApJS*, 214, 15, doi: [10.1088/0067-0049/214/2/15](https://doi.org/10.1088/0067-0049/214/2/15)
- Thorp, S., Alsing, J., Peiris, H. V., et al. 2024, *ApJ*, 975, 145, doi: [10.3847/1538-4357/ad7736](https://doi.org/10.3847/1538-4357/ad7736)
- Thorp, S., Peiris, H. V., Jagwani, G., et al. 2025, *ApJ*, 993, 240, doi: [10.3847/1538-4357/ae0936](https://doi.org/10.3847/1538-4357/ae0936)
- Tong, A., Fatras, K., Malkin, N., et al. 2024, *Trans. Machine Learning Res.*
<https://arxiv.org/abs/2302.00482>
- Tortorelli, L., Fagioli, M., Herbel, J., et al. 2020, *JCAP*, 2020, 048, doi: [10.1088/1475-7516/2020/09/048](https://doi.org/10.1088/1475-7516/2020/09/048)
- Tortorelli, L., Fischbacher, S., Grün, D., et al. 2025, *A&A*, 703, A255, doi: [10.1051/0004-6361/202555759](https://doi.org/10.1051/0004-6361/202555759)
- Tortorelli, L., Bruna, L. D., Herbel, J., et al. 2018, *JCAP*, 2018, 035, doi: [10.1088/1475-7516/2018/11/035](https://doi.org/10.1088/1475-7516/2018/11/035)
- Tröster, T., Asgari, M., Blake, C., et al. 2021, *A&A*, 649, A88, doi: [10.1051/0004-6361/202039805](https://doi.org/10.1051/0004-6361/202039805)
- Virtanen, P., Gommers, R., Oliphant, T. E., et al. 2020, *Nature Methods*, 17, 261, doi: [10.1038/s41592-019-0686-2](https://doi.org/10.1038/s41592-019-0686-2)
- Wang, B., Leja, J., Bezanson, R., et al. 2023, *ApJL*, 944, L58, doi: [10.3847/2041-8213/acba99](https://doi.org/10.3847/2041-8213/acba99)
- Weaver, J. R., Kauffmann, O. B., Ilbert, O., et al. 2022, *ApJS*, 258, 11, doi: [10.3847/1538-4365/ac3078](https://doi.org/10.3847/1538-4365/ac3078)
- Wright, A. H., Hildebrandt, H., van den Busch, J. L., & Heymans, C. 2020, *A&A*, 637, A100, doi: [10.1051/0004-6361/201936782](https://doi.org/10.1051/0004-6361/201936782)
- Wright, A. H., Hildebrandt, H., Kuijken, K., et al. 2019, *A&A*, 632, A34, doi: [10.1051/0004-6361/201834879](https://doi.org/10.1051/0004-6361/201834879)
- Wright, A. H., Kuijken, K., Hildebrandt, H., et al. 2024, *A&A*, 686, A170, doi: [10.1051/0004-6361/202346730](https://doi.org/10.1051/0004-6361/202346730)
- Wright, A. H., Hildebrandt, H., van den Busch, J. L., et al. 2025a, *A&A*, 703, A144, doi: [10.1051/0004-6361/202554909](https://doi.org/10.1051/0004-6361/202554909)
- Wright, A. H., Stözlner, B., Asgari, M., et al. 2025b, *A&A*, 703, A158, doi: [10.1051/0004-6361/202554908](https://doi.org/10.1051/0004-6361/202554908)
- Yoon, M., Hoekstra, H., Li, S.-S., et al. 2025, *arXiv e-prints*, arXiv:2510.01122, doi: [10.48550/arXiv.2510.01122](https://doi.org/10.48550/arXiv.2510.01122)
- Zahid, H. J., Kudritzki, R.-P., Conroy, C., Andrews, B., & Ho, I.-T. 2017, *ApJ*, 847, 18, doi: [10.3847/1538-4357/aa88ae](https://doi.org/10.3847/1538-4357/aa88ae)
- Zahid, H. J., Yates, R. M., Kewley, L. J., & Kudritzki, R. P. 2013, *ApJ*, 763, 92, doi: [10.1088/0004-637X/763/2/92](https://doi.org/10.1088/0004-637X/763/2/92)

APPENDIX

A. MACHINE LEARNING ARCHITECTURES

A.1. *Random forest classifier for detection*

The detection model employs a random forest classifier to predict whether galaxies are detected in the KiDS DR4 r -band observations. Random forests are ensemble learning methods (L. Breiman 2001; F. Pedregosa et al. 2011) that construct multiple decision trees during training and output the class that is the mode of the classes from individual trees. Our implementation uses 100 trees with entropy as the splitting criterion for information gain. The maximum tree depth is set to 37, with a minimum of 12 samples required for splitting and 32 samples per leaf node. The model operates on only two input features: the noiseless r -band magnitude and the GAaP limiting magnitude in the r -band. This simplified feature space reflects the assumption that detection is primarily determined by apparent magnitude and survey depth. The classifier was trained on 800,000 objects randomly sampled from the SKiLLS simulations, producing a binary classification output indicating whether each galaxy would be detected or not detected in the survey.

A.2. *Conditional flow for the uncertainty model*

The uncertainty model predicts the AUTO magnitude error conditioned on the GAaP magnitude error and noiseless magnitude, all in the r -band. This model employs a conditional ODE flow framework (Y. Lipman et al. 2023; A. Tong et al. 2024), which learns to transport samples from a simple base distribution to the target conditional distribution via continuous normalizing flows (R. T. Q. Chen et al. 2018; W. Grathwohl et al. 2019). The architecture consists of a densely connected neural network with four hidden layers, each containing 128 neurons with hyperbolic tangent activation functions. Training proceeds by minimizing the flow matching objective (Y. Lipman et al. 2023) using the Adam optimizer (D. P. Kingma & J. Ba 2015). The conditional flow framework allows flexible modeling of complex conditional probability distributions without restrictive parametric assumptions about the error distribution, while enabling efficient sampling through deterministic ODE integration. All training data comes from detected galaxies in the SKiLLS image simulations, ensuring the learned distribution is conditioned on successful detection.

A.3. *Conditional ODE flow for the noise model*

The noise model generates correlated flux noise residuals across all nine photometric bands ($ugriZYJHK_s$) plus the r -band AUTO flux, conditioned on the noiseless model magnitudes and magnitude limits (equivalent to fluxes and flux uncertainties). The architecture mirrors that of the uncertainty model, using a conditional ODE flow framework (Y. Lipman et al. 2023; A. Tong et al. 2024) with a densely connected neural network consisting of four hidden layers of 128 neurons each and hyperbolic tangent activation functions. However, the input dimensionality is substantially larger at 20 dimensions: nine noiseless magnitudes, ten flux uncertainties (GAaP for nine bands plus AUTO for r -band), and the flow time parameter t . The output is ten-dimensional, providing predictions for the normalized flux residuals. The model is trained using the flow matching objective with the Adam optimizer, exclusively on detected SKiLLS galaxies to ensure proper conditioning on the detection process. By modeling the joint distribution of flux residuals across all bands simultaneously, the conditional flow framework naturally captures inter-band correlations without requiring explicit correlation matrices or parametric assumptions.

A.4. *Random forest classifier for KiDS-1000 selection*

This classifier predicts which galaxies from the parent DR4 catalog pass the quality cuts for inclusion in the KiDS-1000 weak lensing sample. The architecture employs 100 decision trees with entropy-based splitting, maximum tree depth of 37, minimum samples for split of 12, and minimum samples per leaf of 32. The input feature space is substantially richer than the detection model, comprising 20 features: AUTO magnitude, and GAaP magnitudes in all nine bands, their corresponding magnitude uncertainties, and limiting magnitudes derived from the 1σ flux uncertainties. The training set consists of approximately 5 million galaxies split 70/30 for training and testing. During inference, we stochastically assign mock galaxies to the KiDS-1000 sample by drawing from a Bernoulli distribution using the classifier predicted probabilities.

A.5. *Neural network regressor for lensfit weights*

This model predicts *lensfit* shape measurement quality weights from photometric features alone, without access to morphological information or image-level diagnostics. The architecture consists of a fully-connected feed forward neural network with four hidden layers plus one output layer. Each hidden layer contains 128 neurons with hyperbolic

tangent activation functions. The input features are identical to those used in the KiDS-1000 selection classifier: 20 photometric measurements including **GAaP** and **AUTO** magnitudes, their uncertainties, and limiting magnitudes across all nine bands. Input features are standardized using training set statistics, with mean subtraction and division by standard deviation applied consistently during training and inference. The output layer uses a sigmoid activation function to produce values in the range $[0, 1]$, which are then rescaled to $[0, 20]$ using learned normalization parameters to match the target *lensfit* weight range. The model is trained using mean absolute error (MAE) as the loss function rather than mean squared error, as MAE is less sensitive to outliers and better suited for the heavily skewed weight distribution. The **Adam** optimizer (D. P. Kingma & J. Ba 2015) is configured with an initial learning rate of 0.0004 and weight decay of 10^{-4} for L_2 regularization. Several regularization techniques prevent overfitting: a dropout rate of 0.3, batch normalization, and a dynamic batch size scheduling strategy with optimizer restart. The system monitors validation loss for plateaus using a patience of 5 epochs. When a plateau is detected, the batch size increases by a factor of 4 from an initial 512 up to a maximum of 8192, while the learning rate decreases by the same factor. This strategy allows the model to escape local minima and explore different regions of the loss landscape. Training data is restricted to KiDS-1000 galaxies only, with 70% used for training and 30% for validation.